

**A High-Efficiency Open-Winding Induction Motor Drive  
Using a Constant Power Factor Control Scheme**

by

Ian James Smith

A thesis submitted in partial fulfillment of the requirements for the degree of

Master of Science

in

Energy Systems

Department of Electrical and Computer Engineering  
University of Alberta

© Ian James Smith, 2018

UNIVERSITY OF ALBERTA

## *Abstract*

Faculty of Graduate Studies and Research  
Department of Electrical and Computer Engineering

Master of Science

### **A High-Efficiency Open-Winding Induction Motor Drive Using a Constant Power Factor Control Scheme**

by Ian James Smith

Power electronics based variable-frequency drives (VFDs) for electric motors are a widespread technology in industrial settings and commercial products; offering increased functionality, accurate control of speed and torque, and substantial energy savings. A myriad of converter topologies and control techniques exist for a wide range of VFD applications. A high-efficiency control scheme is presented for an open-winding induction motor (OWIM) dual inverter VFD, where primary and secondary inverters are supplied from a DC power source and a floating DC capacitor, respectively. This topology is beneficial as it can produce multilevel pulse-width modulation (PWM) waveforms, eliminates zero-sequence common-mode currents within the system, and extends the motor's constant torque and power regions through voltage boosting. Examination of the equivalent circuit model of an induction motor (IM) reveals that very high motor efficiencies are achieved at a constant motor fundamental power factor over a wide range of motor loads and drive frequencies. Thus, the developed control scheme utilizes the drive's topology to maintain the motor's desired power factor

angle, while also incorporating feedback control of the floating capacitor's voltage. This approach updates the motor's voltage automatically to ensure constant power factor operation and improves the voltage stability of the floating capacitor, while only requiring feedback measurements of the drive's two DC link voltages. In addition, a sensorless slip compensation technique is incorporated into the control algorithm, which utilizes the correlation between the IM's operating power factor and the machine's slip. The inherent voltage boosting capability of this topology is especially beneficial during operation under speed range extension. Experimental testing of the proposed system has verified the predicted steady-state efficiency gains for the induction motor under constant power factor operation as compared with conventional drive control, and has demonstrated stable system performance during both load and speed transients.

# Preface

The original research presented in this thesis has been previously accepted for publication as: I. Smith and J. Salmon, “High efficiency operation of an open-ended winding induction motor using constant power factor control,” *IEEE Trans. Power Electron.*, DOI 10.1109/TPEL.2018.2806740. This publication includes a component of the background and analysis presented in chapter 2, the novel control scheme described in chapter 3, and the majority of the data and results discussed in chapter 4. I was responsible for the design and implementation of the proposed motor control scheme, data collection and analysis, and manuscript composition. Dr. John Salmon was the supervisory author and contributed to concept formation and manuscript edits. The technical apparatus referred to in chapter 4 was provided by the research group of Dr. John Salmon.

## Acknowledgements

Firstly, I would like to recognize and thank my supervisor, Dr. John Salmon, for his support, guidance, and expertise throughout my graduate program. As an extremely accessible supervisor, he allowed me to pursue my research goals while providing welcomed advice and input along the way. The opportunities that he granted me directly led to valuable internship experience, and for that I will always be grateful.

Albert Terheide and Reaz Ul Haque also deserve a big thank you for their technical support, helpful demeanor, and friendliness in the lab.

My family has always extended their unwavering support no matter the endeavor I am pursuing. Thank you to my parents, Ron and Debbie, for placing me in positions to succeed from a young age, and providing me with the confidence to strive for my goals. Thank you to my brother, Brendan, for your always sound advice, but most importantly your friendship. And thank you to Stephanie, for being the best partner I could ask for, and making Edmonton feel like home these last three years.

Lastly, I would like to thank the National Science and Engineering Research Council of Canada, Alberta Innovates, and the University of Alberta for their funding and monetary support towards my research, without which this thesis would not have been possible.

– IJ Smith, February 2018

# Table of Contents

<b>Abstract</b>	<b>ii</b>
<b>Preface</b>	<b>iv</b>
<b>Acknowledgments</b>	<b>v</b>
<b>Table of Contents</b>	<b>vi</b>
<b>List of Tables</b>	<b>viii</b>
<b>List of Figures</b>	<b>ix</b>
<b>1 Introduction .....</b>	<b>1</b>
1.1 Applications of Variable-Frequency Motor Drives .....	2
1.2 Conventional Drive Control of Induction Motors.....	3
1.2.1 Constant Volts-per-Hertz Control .....	5
1.2.2 Field-Oriented Control.....	8
<b>2 The Open-Winding IM Dual Inverter Drive.....</b>	<b>10</b>
2.1 Topology Configurations of the Dual Inverter Drive .....	11
2.2 The Dual Inverter Drive using Two Isolated DC Sources.....	12
2.3 The Dual Inverter Drive using a Single DC Source.....	12
2.4 The Dual Inverter Drive using a Floating Capacitor Bridge.....	16
<b>3 Power Factor Control for High Motor Efficiencies.....</b>	<b>23</b>
3.1 Achieving High Efficiencies at a Constant Power Factor.....	24
3.2 The Power Factor Controller for the Dual Inverter Drive.....	28
3.2.1 A Sensorless Method for Slip Compensation.....	32
3.2.2 System Start-Up Procedure.....	32

<b>4</b>	<b>System Results and Performance Analysis .....</b>	<b>34</b>
4.1	Experimental Setup .....	35
4.2	System Start-Up .....	36
4.3	Steady-State System Performance .....	37
4.4	System Performance During Load Transients .....	43
4.5	System Performance During Speed Transients.....	45
<b>5</b>	<b>Conclusion .....</b>	<b>48</b>
5.1	Suggestions of Future Work.....	49
	<b>References.....</b>	<b>52</b>

## List of Tables

2.1	Switching state table for the dual inverter drive .....	13
2.2	Zero-sequence voltage injections of the switching states .....	15
4.1	Parameters of the test induction motor .....	35

## List of Figures

1.1	Reduction in power consumption due to a speed decrease in a fan load .....	2
1.2	Single-phase simplified equivalent circuit model for the induction motor .....	4
1.3	Basic topology of an induction motor variable-frequency drive .....	5
1.4	Modified IM equivalent circuit model including V/f assumptions .....	6
1.5	Typical V/f profile for volts-per-hertz motor control .....	7
1.6	Closed-loop V/f control with a PI compensator .....	7
1.7	Rotor-field oriented vector control of an induction motor .....	9
2.1	Configurations of the dual inverter drive .....	11
2.2	The switches of the dual inverter drive with a single DC source .....	13
2.3	Example switching states of the floating bridge topology demonstrating capacitor charging, discharging, and maintaining previous charge .....	18
2.4	The voltage phasors of the dual inverter drive .....	19
2.5	The natural charging process of the floating capacitor .....	21
2.6	The natural discharging process of the floating capacitor .....	21
3.1	The exact per-phase equivalent circuit model of the open winding induction motor .....	25
3.2	Theoretical motor efficiencies .....	27
3.3	Power factors for optimal efficiency operation for a 5 HP experimental motor ....	28
3.4	Steady-state space-vector diagram for the proposed controller .....	29
3.5	Control block diagram of the proposed power factor controller .....	31

3.6	Control block diagram of the soft-start algorithm .....	33
4.1	Experimental setup .....	35
4.2	Simulation results: (a) RMS motor voltage and (b) RMS motor current during soft-start .....	36
4.3	Experimental results: capacitor pre-charging .....	37
4.4	Experimental results: motor efficiencies under V/f control and constant power factor control compared with the theoretical maximum efficiency .....	38
4.5	Experimental results: motor current comparison between constant power factor control, V/f control, and the theoretical maximum efficiency operation .....	40
4.6	Experimental results: (a) motor phase RMS voltage and (b) floating capacitor voltage of the dual inverter drive under constant power factor control .....	41
4.7	Experimental results: motor RPM slip comparison between constant power factor control and V/f control methods .....	42
4.8	Experimental results: power losses in the main and floating bridges .....	43
4.9	Simulation results: (a) load torque; (b) capacitor voltage and reference; (c) motor phase voltage; (d) power factor angle; (e) motor speed and reference .....	44
4.10	Experimental results: floating capacitor voltage during load transients .....	44
4.11	Experimental results: (a) modulation index, $m_I$ ; (b) phase voltages $ \vec{v}_1 $ and $ \vec{v}_2 $ ; (c) RMS motor current, $ \vec{i}_s $ .....	45
4.12	Simulation results: (a) motor speed and reference; (b) capacitor voltage and reference; (c) motor phase voltage; (d) motor power factor angle .....	46
4.13	Experimental results: floating capacitor voltage during speed transients .....	46
4.14	Experimental results: (a) modulation index, $m_I$ ; (b) phase voltages $ \vec{v}_1 $ and $ \vec{v}_2 $ ; (c) RMS motor current, $ \vec{i}_s $ .....	47

# Chapter 1

## Introduction

Power electronics converters, and particularly voltage-source converters (VSCs), are a fundamental building block of the modern power system, enabling emerging renewable energy technologies, high-efficiency motor drive systems, and a multitude of utility level applications. Research is continuously being conducted regarding new topologies and control systems for VSC applications, striving for economical solutions that improve upon the efficiency and robustness of previous iterations. The contribution of this work is to present a control scheme for an open-winding induction motor (OWIM) dual inverter drive (DID) system. The proposed control utilizes the inherent characteristics of the drive topology to automatically maintain the optimal rated motor power factor (PF) over the entire load and speed range of the machine, thus ensuring energy savings under high-efficiency operation. This chapter introduces the concept of variable-frequency motor drives while providing context, justification, and applications for the work. Chapter 2 and Chapter 3 examine the DID topology in detail, and present the key conceptual contributions of the proposed control method.

## 1.1 Applications of Variable-Frequency Motor Drives

When Nikola Tesla invented and patented the electric induction motor in 1888 he revolutionized society's industrial, manufacturing, and commercial sectors for centuries to come. Today, electric motors are the single largest consumer of electrical power in the United States, accounting for 60-65 percent of all grid energy [1,2]. On a global scale, electric motors consume 66 percent of electrical power used by industry, representing approximately 25 percent of all electricity consumed worldwide [3]. This staggering amount of energy is utilized to power a wide range of applications, from small household appliances to large industrial applications such as fans, pumps, compressors, and mixers. In the coming decades, the energy consumption of electric motors is projected to increase significantly, as electric vehicles (EVs) continue to increase their market share against conventional gas-powered alternatives.

Variable-torque loads, such as fans and pumps, are common applications for electric motors, in which the torque placed on the motor is highly dependent on the motor's speed. In many of these applications, the torque is characterized by an exponential relationship to the speed, typically to the second or third degree. Thus, a small reduction in speed may result in a substantial reduction in both the motor's torque and power consumption. For example, a load with a cubic relationship to the motor's speed will consume 33 percent less power with just a 10 percent speed reduction, see Fig. 1.1.

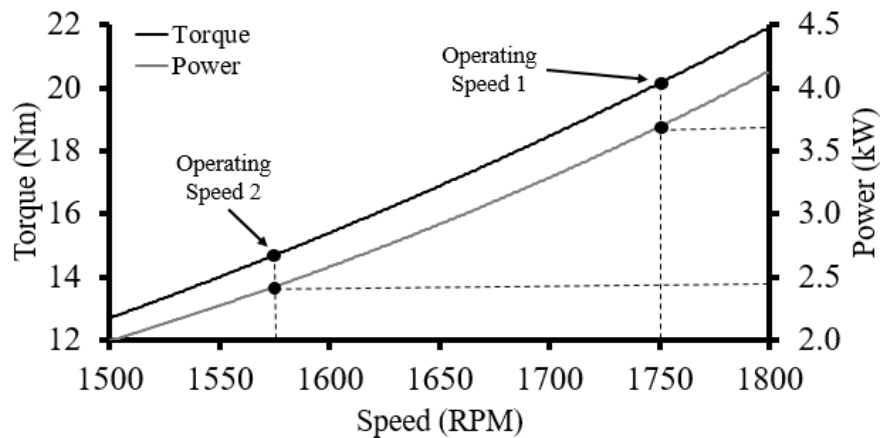


Fig. 1.1 Reduction in power consumption due to a speed decrease in a fan load

Other electric motor applications, such as EVs, demand accurate control of the motor's torque and speed, along with fast and stable dynamic response characteristics. Both applications may utilize power electronics based variable-frequency drives (VFDs) to meet the demands of the application. VFDs use power converters to regulate the frequency, phase, and magnitude of the ac voltage supplied to the motor, thus accurately controlling the motor's speed and torque operating point. If a motor is directly connected to the grid, its synchronous speed is locked to the grid frequency. Under this scenario, if a fan or pump is to have a reduced throughput, the medium being transported must be mechanically throttled. Meanwhile, the motor remains operating at the grid frequency and voltage consuming unnecessarily large amounts of power. Further benefits of VFDs include increased functionality, such as soft-starters and voltage droop compensators. Currently, only 3 percent of installed AC motors are paired with VFDs [4]; however, approximately 35 percent of newly installed motors incorporate a drive system [5]. Regarding the 40 million variable-torque loaded motors in the United States, it is estimated that the widespread implementation of VFDs could reduce their energy consumption by 18 percent [6].

## **1.2 Conventional Drive Control of Induction Motors**

The three-phase induction motor (IM) is the workhorse of modern industry due to its relatively low cost, ruggedness, reliability, and high power conversion efficiency. To understand conventional drive control methods, the basic operating principles of the IM should first be understood. A three-phase squirrel-cage IM is constructed of a stator and a rotor, separated by a small air gap. The stator houses the three phase windings, spatially shifted by 120 electrical degrees. When energized by an ac source at steady-state, these windings produce a rotating magnetic field which has a constant amplitude and angular velocity. This magnetic flux cuts through the conductors of the rotor, inducing a current-generating back emf as per Faraday's Law. As the conductors in the rotor are short-circuited, a rotor current will begin to flow. A current-carrying conductor moving through a magnetic field experiences a Lorentz force perpendicular to both the current's direction and the field, thus creating a torque which

turns the rotor. The rotor will accelerate until the torque induced by the rotating magnetic field matches the load torque placed upon the motor. However, if the rotor were to revolve at the same frequency as the stator's magnetic field, then no magnetic force could be generated on the rotor. For this reason, IMs operate at speeds slightly below the supply frequency, as slip must occur between the stator's magnetic field and the rotor. As the motor's load torque is increased, the rotor will slow down causing its conductors to be cut by more magnetic flux. Therefore, the current induced in the rotor will also become greater as the slip of the motor is increased. The electrical behaviour of the induction machine is often emulated using the simplified single-phase equivalent circuit model, see Fig. 1.2.

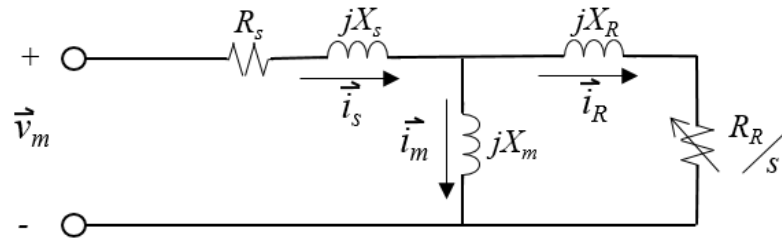


Fig. 1.2. Single-phase simplified equivalent circuit model for the induction motor

$R_S$  and  $X_S$  are the stator impedances,  $R_R$  and  $X_R$  are the rotor impedances,  $X_m$  is the magnetizing branch impedance,  $\vec{v}_m$  is the per-phase supply voltage, and  $s$  is the motor's operating slip.  $\vec{i}_s$ ,  $\vec{i}_m$ , and  $\vec{i}_r$  are the space-vector representations of the motor's stator, magnetizing, and rotor currents, respectively. The machine's synchronous rpm speed and slip are defined by (1.1) and (1.2), respectively.

$$n_s = \frac{120f}{p} \quad (1.1)$$

$$s = \frac{n_s - n}{n_s} \quad (1.2)$$

Where  $f$  is the machine's supply frequency,  $p$  is the number of magnetic poles, and  $n$  is the rpm of the rotor. Power losses in the IM can be categorized as conduction losses in the stator and rotor, friction and windage losses, and core or magnetizing losses in the laminated steel of the stator. Through varying the voltage magnitude supplied to the stator's windings, the ratio between the magnetizing and rotor currents of the equivalent circuit can be modified, thus allowing the motor's power factor to be controlled for improved motor efficiencies.

The typical topology of a grid-connected VFD consists of three primary components: a rectifier stage, the DC-link, and an inverter stage, see Fig. 1.3. The input stage is typically a three-phase diode rectifier, or an active front-end converter if regenerative braking is desired. The DC-link capacitor maintains a constant DC voltage, bridging the gap between the rectifier and inverter. Lastly, the inverter supplies the motor with variable magnitude and variable frequency ac voltage based upon the control objectives. Multiple methods exist for controlling the inverter, however the clear majority are based upon the well-known switching concept of pulse-width modulation (PWM). In three-phase sinusoidal PWM, three reference sinusoids separated by 120 degrees, with magnitudes between 0 and 1, are compared to a high-frequency triangular carrier waveform. These comparisons generate the gating signals sent to the inverter's switches, which provide either the DC-link voltage or zero volts to the stator's windings. Turning the switches on/off at varying duty-cycles is done such that the high-frequency voltage pulses encode the desired phase, frequency, and magnitude of the PWM sinusoidal reference signal. The frequency of the switching pulses is great enough such that the filtered average, or fundamental, of the signal is very close to a pure sinusoid, containing minimal harmonics.

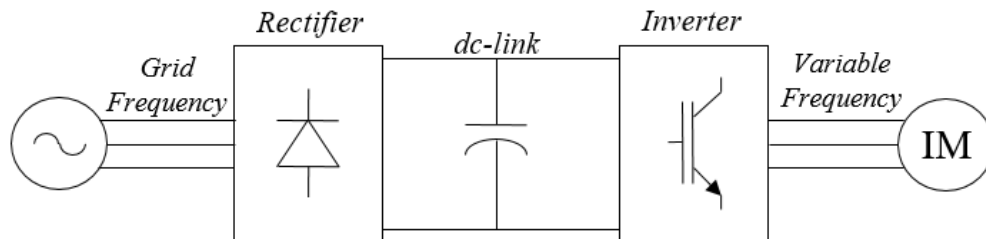


Fig. 1.3. Basic topology of an induction motor variable-frequency drive

### 1.2.1 Constant Volts-per-Hertz Control

$V/f$  control, also known as scalar control, is the simplest method of controlling an IM drive. It is known as a scalar control method as the drive is solely concerned with the magnitudes of the voltage and frequency supplied to the motor. Benefits of  $V/f$  control include the ease of implementation and accurate speed control of the motor under steady-state conditions. However, the simple nature of this control makes it susceptible to slow dynamic

responses and instability at very low speeds. Consider a modified equivalent circuit model of the induction motor, in which the stator's resistance is assumed to be zero, and the stator's leakage inductance is lumped together with that of the rotor, see Fig. 1.4.

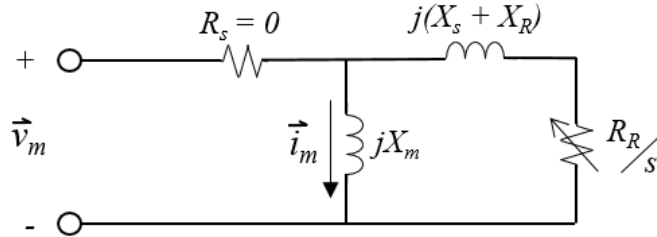


Fig. 1.4. Modified IM equivalent circuit model including V/f assumptions

The magnetizing current,  $I_m$ , in the above model is the current which provides the magnetic flux linkage between the stator and the rotor. Based upon the assumptions made in Fig. 1.4, the magnetizing current may be estimated as:

$$|\vec{i}_m| = \frac{|\vec{v}_m|}{X_m} = \frac{|\vec{v}_m|}{2\pi f L_m} \propto \frac{|\vec{v}_m|}{f} \quad (1.3)$$

The machine parameter  $L_m$  remains constant during normal operation. Thus, if the  $V/f$  ratio of the supply voltage is kept constant, the magnitude of the flux-inducing magnetizing current will also remain constant. This is the general idea behind  $V/f$  control: maintain the volts-per-hertz ratio achieved at rated conditions, such that the optimal flux linkage is maintained at a constant value for all steady-state operation, see Fig. 1.5. This allows for the delivery of constant torque over the entire speed range of the motor. At very low speeds and voltages, the assumption that the stator resistance,  $R_s$ , produces a negligible voltage drop becomes invalid. Therefore, typical  $V/f$  profiles often contain a voltage boost at low speeds, to provide a sufficient voltage to the magnetizing branch in the equivalent circuit model and avoid stalling the motor. At speeds beyond the rated motor speed, the supply voltage magnitude is often capped to avoid damaging the stator's insulation, however this depends on the tolerances of a given motor.

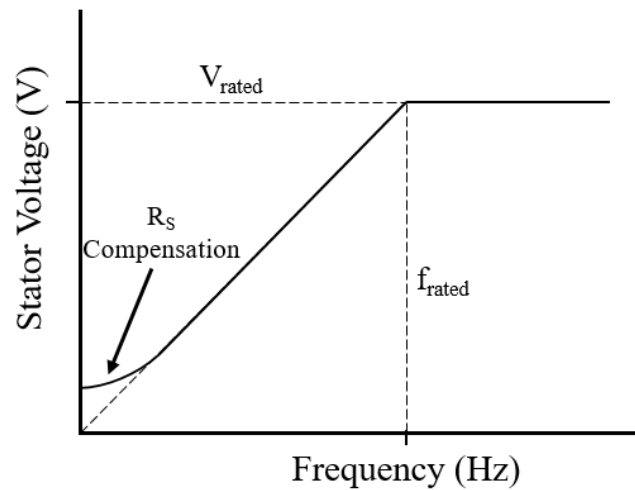


Fig. 1.5. Typical V/f profile for volts-per-hertz motor control

Under open-loop  $V/f$  control, the slip of the rotor is not considered when providing the supply frequency to the motor. Thus, between no-load and full-load the slip increases, which in turn has a small impact on the torque production of the motor. The slip range of a typical IM will vary between approximately 0.1 percent of the rated speed at no-load, and up to 3 percent at full-load. In applications in which precise steady-state speed control is unnecessary, this is a suitable implementation of  $V/f$  control. However, in more demanding applications a speed encoder or resolver may be added to the motor, coupled with slip compensating closed-loop feedback, see Fig. 1.6.

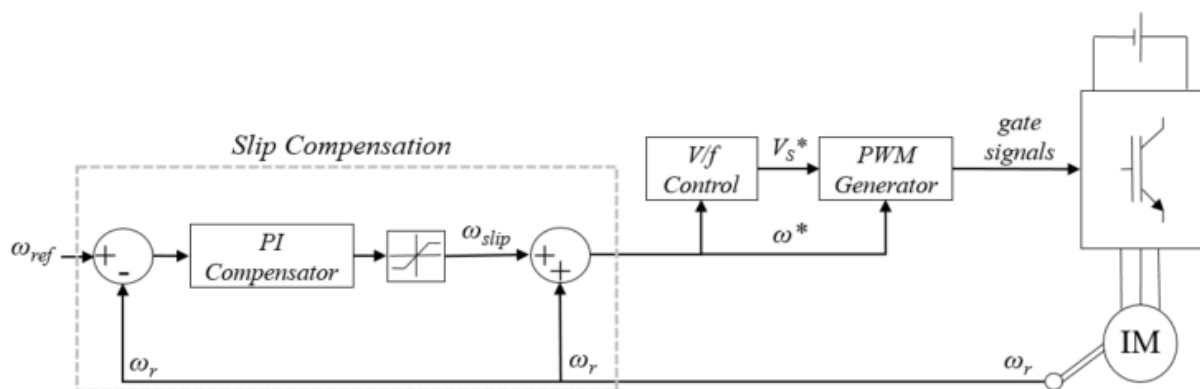


Fig. 1.6. Closed-loop V/f control with a PI compensator

In closed-loop  $V/f$  control, the actual rotor speed is compared to the reference speed using a negative feedback loop. The speed error is typically supplied to a PI compensator, utilized to minimize the error caused by the rotor's slip. The boosted reference frequency and corresponding voltage magnitude is then supplied to the PWM generator. Thus, the load-dependent slip of the motor is accounted for, providing accurate steady-state speed regulation.

## 1.2.2 Field-Oriented Control

Field-oriented control (FOC), also known as vector or current control, is a more advanced form of machine control based on the manipulation of the stator's current vectors. This method of control is more complex, having higher computing demands, while providing improved dynamic characteristics, stability, and feedback responses. Using the space-vector representation for the machine, and the applicable Clarke or Park transformations, the motor may be modeled in either a two-phase stationary reference frame or rotating reference frame, respectively. In the rotating dq-frame of reference, the magnetic flux and torque of the motor may be decoupled, allowing for linear feedback control similar to that of a DC excited motor. The dq-frame may be synchronized with the magnetic field's of either the rotor or stator, resulting in rotor-field oriented (RFO) or stator-field oriented (SFO) control. Considering RFO control, the flux of the rotor is aligned with the d-axis of the reference frame, such that the supplied q-axis stator current magnitude regulates the electromagnetic torque produced in the motor.

Similar to the less complex  $V/f$  control method, the primary goal of FOC is to maintain the rated rotor flux in order to maximize torque production throughout the motor's entire range of operation. In other words, the magnitude of the current in the equivalent circuit model's magnetizing branch is maintained such that the motor's overall losses are minimized, and the optimal torque-per-amp value is achieved. In the case of squirrel-cage IMs where the rotor is electrically isolated, this goal is achieved through the precise control of the stator's current vectors in the dq-frame, Fig. 1.7. Two nested PI control loops are utilized for decoupled feedback control of the motor's torque ( $\tau$ ) (q-axis loop) and flux ( $\lambda$ ) (d-axis loop), as PI

compensators are effective in regulating the DC values of the rotating reference frame. The rotor's flux ( $\lambda_r$ ) and angular position ( $\theta_r$ ) must be known in order to complete the flux feedback control loop and perform the necessary Park transformations. Typically, this is achieved through either resolver speed/position feedback measurements, voltage integration calculations using measured stator current and voltage values, or through using a closed-loop state-observer model. Without entering into many details, observer models estimate stator and rotor state variables based upon measured current values and the voltages being supplied to the motor. Common practice is to measure two stator currents and calculate the third based upon a three-wire system. The common method of field-weakening is often applied in conjunction with vector control for the applications that demand motor speeds beyond the rated speed of the machine. Once the maximum voltage operating point of the drive has been reached, due to device limits or a limited supply voltage, the motor's flux may be independently decreased such that the maximum possible torque-per-amp output can be achieved into the speed range extension region.

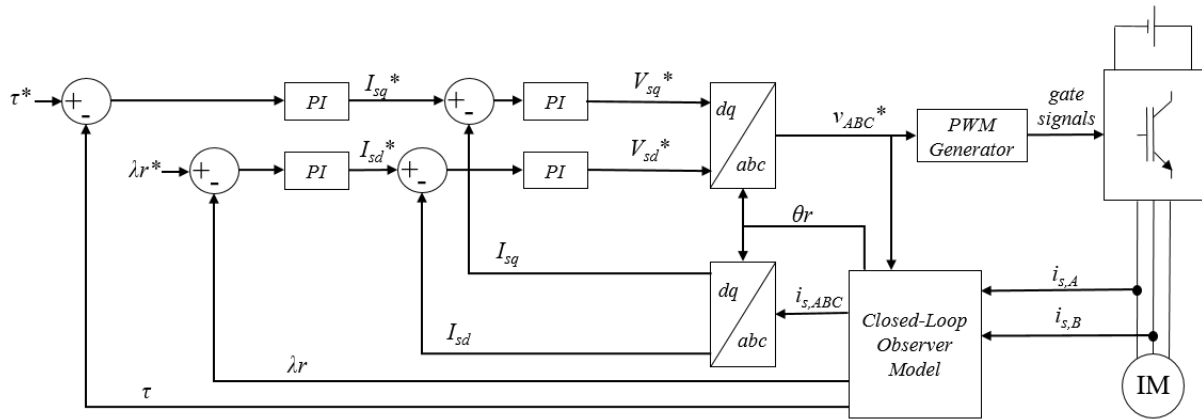


Fig. 1.7. Rotor-field oriented vector control of an induction motor

## **Chapter 2**

# **The Open-Winding IM Dual Inverter Drive**

This thesis presents a controller for an OWIM DID which utilizes a floating capacitor bridge on the secondary side of the induction motor. Over the last decade, the DID topology has gained attention as a practical multi-level variable-frequency motor drive system. Similar to the well-known neutral-point clamped (NPC) converter, the DID topology is capable of supplying five-level line PWM voltage waveforms [7-20], while requiring the same number of switches, fewer diodes, and a less complex control without capacitor voltage balancing. The other primary benefit of this topology is its capability to boost the motor's supply voltage beyond the maximum base voltage from a single DC source [21-24]. These characteristics make the DID ideal for medium voltage and high power applications, or low voltage applications demanding high speeds [25-27]. Three configurations of the DID topology have been studied in literature, each with their own specific benefits and challenges: using two isolated DC sources, using a single DC source to supply both inverters, and using a floating DC capacitor to supply the secondary bridge. This chapter reviews the configurations of the DID in terms of topology, principles of operation, and control methods, while detailing the benefits and disadvantages in each case.

## 2.1 Topology Configurations of the Dual Inverter Drive

Three primary configurations of the DID coupled with open-winding machines have been discussed in literature: the use of two isolated DC sources, a single DC source for both converters, and a floating DC capacitor to supply a floating secondary bridge, see Fig. 2.1.  $\vec{v}_1$  and  $\vec{v}_2$  are the space-vector representations of the RMS phase voltages injected by the primary and secondary bridges, respectively.  $\vec{v}_2$  is considered in the negative direction relative to  $\vec{v}_1$ , such that the per-phase voltage supplied to the stator,  $\vec{v}_m$ , is the vector sum of  $\vec{v}_1$  and  $\vec{v}_2$ .

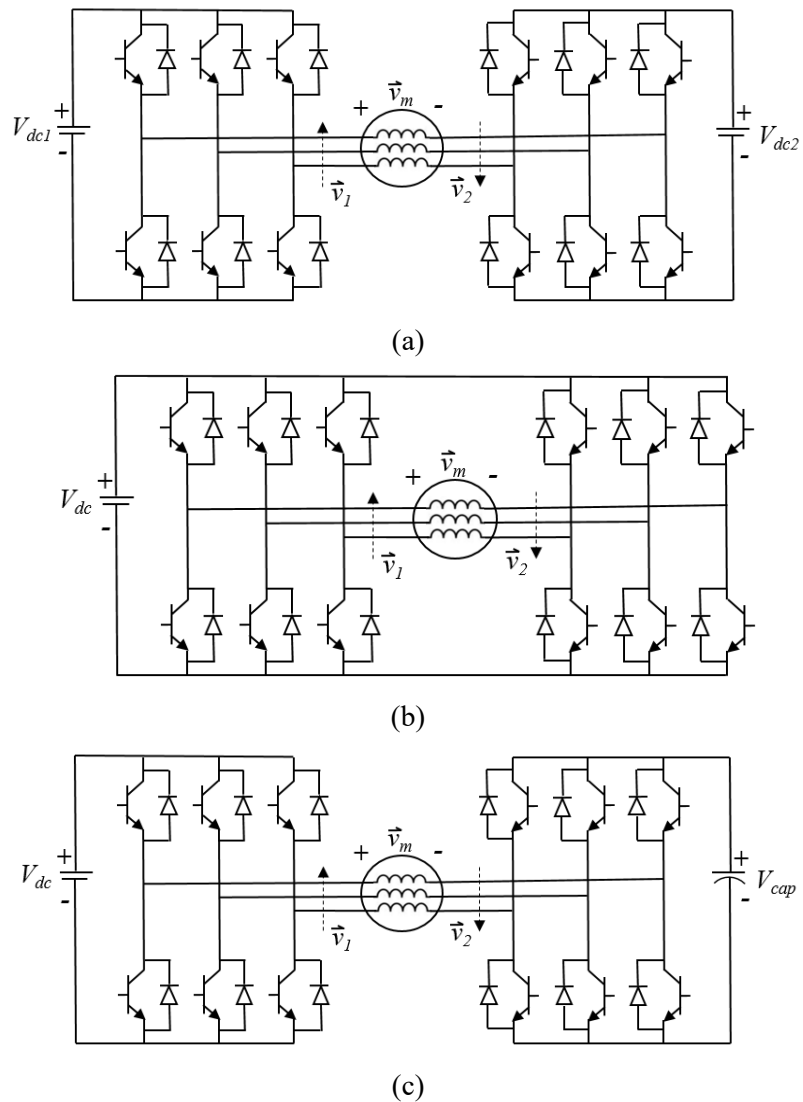


Fig. 2.1. Configurations of the dual inverter drive (a) two isolated DC sources (b) single DC source (c) floating capacitor bridge

## 2.2 The Dual Inverter Drive using Two Isolated DC Sources

In Fig. 2.1(a), two electrically isolated sources supply separate three-phase two-level inverters positioned on the primary and secondary terminals of an open-winding motor. The two sources may be purely DC components, such as batteries, or independent DC-links which have been rectified from a common AC source via isolating transformers. Multiple space-vector modulation techniques have been proposed for providing multilevel PWM voltage waveforms using this configuration, demonstrating similar waveforms as other common three-level topologies, such as the NPC and coupled-inductor inverters [17-19,28]. Multilevel voltages are beneficial as they allow for a decreased switching frequency, while keeping the harmonic content in the resulting current waveforms low. Furthermore, multilevel PWM decreases the  $dv/dt$  stresses on the individual transistors and lowers the electromagnetic interference (EMI) emitted by the converter. Another benefit of this configuration is the voltage boosting available to the motor, as the voltage magnitude capability of this topology is double that of a single inverter drive with a similar DC source. This increases the voltage limitation of the drive, extends the speed range of the motor, and decreases the requirement for flux weakening. However, this topology necessitates a more complex control scheme, as power balancing between the two inverters is required to balance the two DC voltages and result in equivalent device lifetimes [17,18]. The main drawback of this topology compared to the other two DID configurations stems from the necessity of two isolated sources. Including two batteries, or alternatively two isolating transformers and rectifiers, in this drive increases the size, weight, and cost of the system compared to a DID supplied by a single source [21].

## 2.3 The Dual Inverter Drive using a Single DC Source

A simple solution to overcome the added cost and bulk of two isolated DC sources is to supply both the primary and secondary bridges from a single source [11-14,29,30]. Through applying a phase shift between the fundamental voltage injections of the two inverters, the benefit of voltage boosting may still be realized while also allowing for multilevel PWM. However, in connecting the DC link of both inverters, pathways for zero-sequence, or common

mode, currents are created within the system. While zero-sequence currents (ZSCs) do not contribute to the developed electromagnetic torque, they can lead to undesirable effects such as increased conduction losses and torque ripple, and thus should be suppressed. The primary cause of ZSCs in this topology configuration is the creation of zero-sequence voltages (ZSVs) due to some switching states. Consider the single DC source DID topology as denoted in Fig. 2.2.

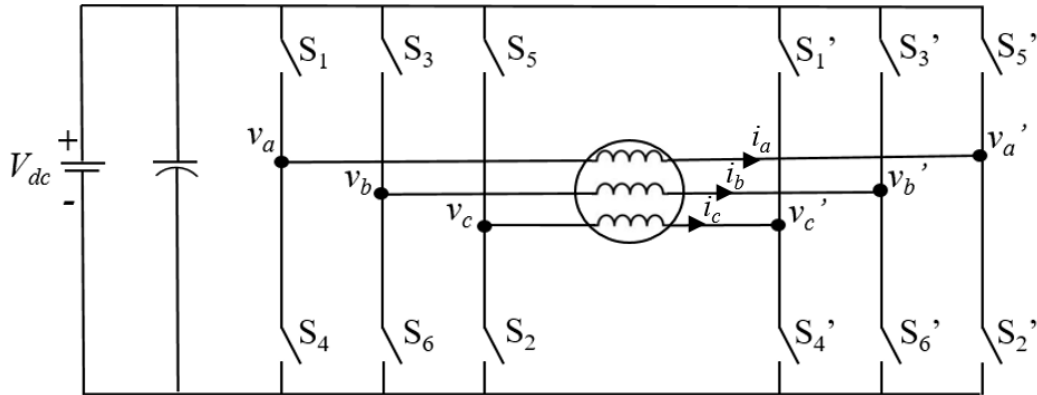


Fig. 2.2. The switches of the dual inverter drive with a single DC source

As only one switch of an inverter leg may be on at a given time, each of the classic six-switch inverters in Fig. 2.2 has eight possible switching states, resulting in a total of 64 switching states when coupled together in the DID topology, see Table 2.1.

Table 2.1. Switching state table for the dual inverter drive

Primary Bridge		Secondary Bridge	
Switching State	Active Switches	Switching State	Active Switches
1 (100)	S1 S6 S2	1' (100)	S1' S6' S2'
2 (110)	S1 S3 S2	2' (110)	S1' S3' S2'
3 (010)	S4 S3 S2	3' (010)	S4' S3' S2'
4 (011)	S4 S3 S5	4' (011)	S4' S3' S5'
5 (001)	S4 S6 S5	5' (001)	S4' S6' S5'
6 (101)	S1 S6 S5	6' (101)	S1' S6' S5'
7 (111)	S1 S3 S5	7' (111)	S1' S3' S5'
8 (000)	S4 S6 S2	8' (000)	S4' S6' S2'

The applied convention uses a ‘1’ to denote the upper switch being on in an inverter leg such that the phase output voltage is equal to  $V_{dc}$ , whereas a ‘0’ denotes the lower switch being active and a phase output voltage of zero. According to the well-known theory of Symmetrical Components in three-phase power systems, the instantaneous zero-sequence component in an unbalanced system may be calculated as follows:

$$V_0 = \frac{1}{3}(V_A + V_B + V_C) \quad (2.1)$$

Thus, the ZSVs applied across the stator’s windings by the inverters, and the resulting ZSCs, are dependent on the current switching state of the inverters, and may be expressed as [14]:

$$v_{s0} = \frac{1}{3}(v_{aa'} + v_{bb'} + v_{cc'}) \quad (2.2)$$

$$i_{s0} = \frac{1}{3}(i_a + i_b + i_c) \quad (2.3)$$

$v_{aa'}$ ,  $v_{bb'}$ , and  $v_{cc'}$  are the RMS voltages across each phase of the stator’s windings. The governing equation for the ZSC in the system can be written as follows [11]:

$$L_l \frac{di_{s0}}{dt} = v_{s0} - R_s i_{s0} - v_{emf,0} \quad (2.4)$$

Where  $L_l$  is the motor’s leakage inductance,  $R_s$  is the stator winding resistance, and  $v_{emf,0}$  is the zero-sequence component of the motor’s back emf voltage. Based upon Equation 2.2, the ZSV applied to the open-winding motor may be calculated for each of the 64 switching states of the DID topology. For example, the switching state combination 45’ results in a ZSV injection of  $V_{dc}/3$ :

$$\begin{aligned} v_{aa'} &= v_a - v_{a'} = 0 - 0 = 0 \\ v_{bb'} &= v_b - v_{b'} = V_{dc} - 0 = V_{dc} \\ v_{cc'} &= v_c - v_{c'} = V_{dc} - V_{dc} = 0 \\ v_{s0} &= \frac{1}{3} (0 + V_{dc} + 0) = \frac{V_{dc}}{3} \end{aligned}$$

The resulting ZSV injections for all 64 switching states of the DID topology are summarized in Table 2.2.

Table 2.2. Zero-sequence voltage injections of the switching states [modified from 14]

$-V_{dc}$	$-2V_{dc}/3$	$-V_{dc}/3$	$0$	$V_{dc}/3$	$2V_{dc}/3$	$V_{dc}$
87'	84'	85' 83' 54'	88' 55' 53'	58' 38' 45'	48'	78'
	86'	34' 81' 56'	35' 33' 44'	43' 41' 18'	68'	
	82'	52' 36' 32'	51' 31' 46'	65' 63' 25'	28'	
	57'	47' 14' 16'	42' 15' 13'	23' 74' 61'	75'	
	37'	12' 67' 27'	64' 24' 11'	21' 76' 72'	73'	
	17'		66' 62' 26'		71'	
			22' 77'			

Multiple strategies have been proposed to mitigate the ZSCs in the single DC source DID topology. Common-mode choke inductors have been added in series with the stator's windings in order to throttle the unwanted currents [21], at the expense of adding extra bulky passive components to the system. Several unique PWM schemes have been proposed which altogether avoid the switching states that result in a zero-sequence component [12,20], limiting the PWM design to just 20 switching states. The main drawback of this approach is a decreased capability to utilize the DC bus voltage [7]. In addition, the ZSCs may be minimized by controlling the ZSV components to equal zero on average over each sampling interval [14]. However, while the mentioned techniques are effective at suppressing the ZSCs due to the inverter's switching states, other sources of common-mode ZSCs exist within the system. Primarily, the necessary dead-time intervals in the PWM switching schemes as well as harmonic content in the motor's back emf can contribute to unbalance in the three-phase system [11]; thus, acting as sources for ZSCs. Dead-time, a short time interval between the turn-off and turn-on of complementary switches to avoid current shoot through, injects a square-wave voltage error into the inverter supplied phase voltage. The back emf of common three-phase motors typically contains a third harmonic component due to the physical construction of the machine [11]. This third harmonic is not seen as an issue in conventional electric machines as triplen harmonics are not realized in the phase voltages or currents.

However, in the scenario of an open-winding machine with voltages applied to the primary and secondary terminals, these harmonics may not be cancelled, resulting in ZSCs. A proposed method utilizes an additional proportional-resonant controller in addition to the existing FOC scheme in order to suppress the overall zero-sequence component within motor drive [11]. The DID configuration with a single DC source offers an effective multi-level converter topology with an additional level of complexity in both the PWM switching and control algorithms to suppress the creation of circulating ZSCs within the system.

## 2.4 The Dual Inverter Drive using a Floating Capacitor Bridge

The DID topology using a floating capacitor bridge sources power from a single DC source connected to the three-phase inverter on the motor's primary terminals. The inverter connected to the motor's secondary terminals utilizes an isolated capacitor to form an additional DC bus, see Fig 2.1(c). Once charged, the isolated capacitor provides a secondary voltage injection to the motor. As there is no common DC bus between inverters, the previous pathways for circulating common-mode currents are eliminated. The effect of the non-grounded floating bridge, with a stable capacitor voltage, is to create a physical neutral point in the three-phase system, thus forcing a set of balanced three-phase currents:

$$i_{s0} = \frac{1}{3}(i_a + i_b + i_c) = 0 \quad (2.5)$$

Therefore, the DID topology with a floating bridge eliminates the need for bulky common-mode choke inductors or an additional level in the PWM control scheme to suppress the zero-sequence currents. This topology also maintains the inherent benefits of the other DID topologies, such as boosting of the motor's terminal voltage, five-level PWM waveforms with increased switching frequency, extension of the constant torque region, and improved motor performance beyond base speed with less flux weakening. Furthermore, the floating bridge topology reduces the size, weight, and cost of the system compared to a DID supplied by two isolated DC sources [21].

The DID topology with a floating bridge has been shown in literature to be an attractive VFD system for various applications. The voltage boosting capability of the secondary bridge has successfully counteracted supply voltage droop, while providing reactive voltage support to the motor [24]. Useful in responding to either variable battery voltage profiles or voltage sag in the distribution network. The design has been demonstrated as a practical high-efficiency multilevel converter topology using both open-loop  $V/f$  and closed-loop flux oriented controllers [7]. Furthermore, the drive has been tested under RFO control in order to demonstrate torque and power improvements in the field weakening region for high speed applications [31, 32].

While the elimination of common-mode current pathways simplifies the necessary control scheme for the system, the charging and discharging of the floating capacitor introduces an additional level of control complexity. It is necessary to regulate the capacitor's voltage in order to ensure stable system behaviour and avoid potentially damaging voltage spikes, especially throughout transient operation. The charging and discharging of the floating capacitor may be considered in the instantaneous manner during each switching cycle, or in the average sense over many switching cycles. First, consider the charging and discharging of the capacitor as it depends on each individual switching state. Fig. 2.3 demonstrates the path and direction of current flow within the system for three example switching states. While the depicted switching states in Fig. 2.3 demonstrate the direction of power flow supplied or absorbed by the floating capacitor, the power balance for the entire system is not considered, as the motor has been omitted from the figure. The switching states are once again denoted by the convention defined in Table 2.1.

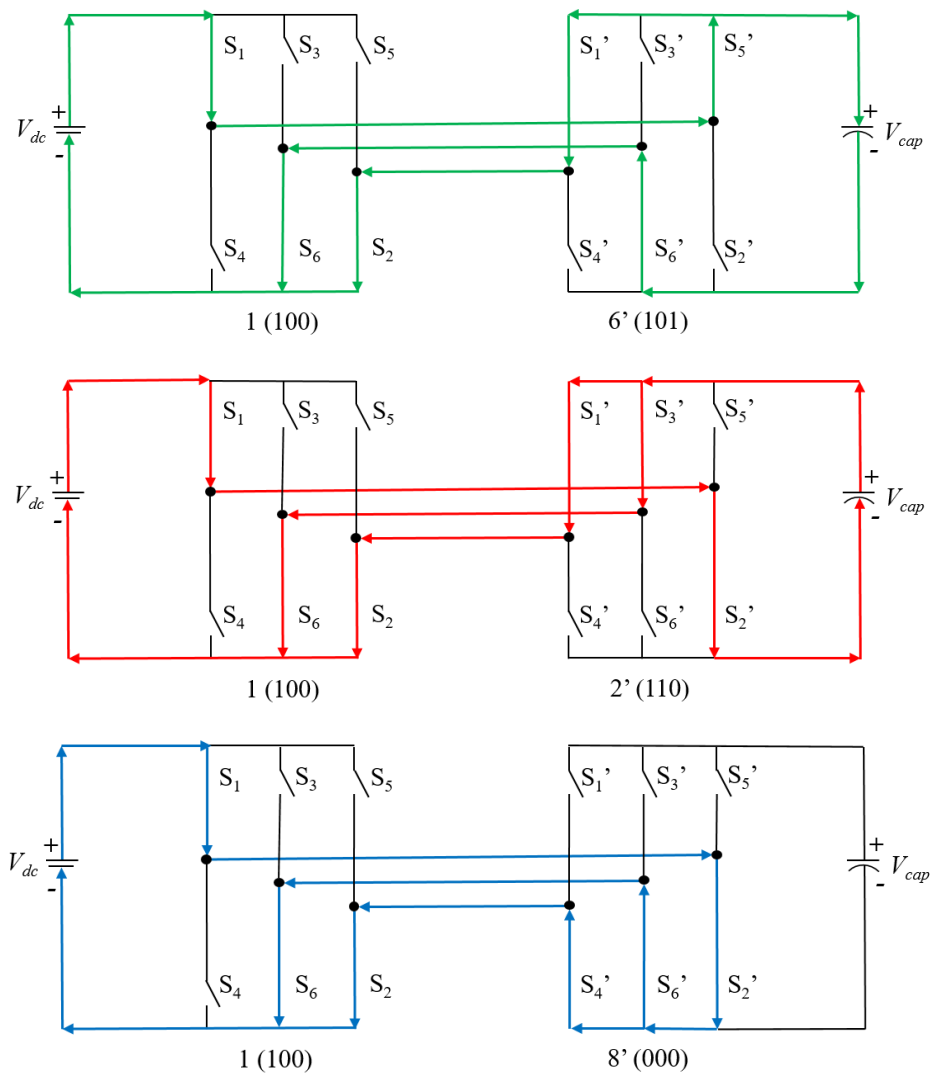


Fig. 2.3. Example switching states of the floating bridge topology demonstrating capacitor charging (16'), discharging (12'), and maintaining previous charge (18') [modified from 7]

The switching state 16', pictured above, results in current flow (denoted by the colour green) into the positive terminal of the floating capacitor, thus charging the capacitor and causing its voltage to increase. Alternatively, switching state 12' results in current flow (denoted by the colour red) out of the capacitor's positive terminal, resulting in discharging. Lastly, switching state 18' isolates the floating capacitor from the flow of current (denoted by the colour blue), allowing the capacitor to remain at its previous state of charge. Knowledge of the capacitor's charging behaviour during each switching state, and the existence of redundant switching states, allows for the design of multilevel switching schemes which also regulate the floating

capacitor's voltage. A modified space-vector PWM method has been proposed, which provides five-level line voltages to the motor while regulating the capacitor voltage at 50% relative to the main DC supply voltage [7]. A similar control scheme utilizing a model-predictive controller has been presented which eliminates the need for the dwell-time calculations and switching sequence design seen in space-vector PWM [8].

The charging behaviour of the floating capacitor may also be considered in the average sense over many switching cycles, utilizing the phasor relationships between the drive's voltages and currents. The drive's RMS voltage space-vectors  $\vec{v}_1$  and  $\vec{v}_2$ , Fig. 2.1(c), represent the two components of the motor's per-phase fundamental voltage resulting from the main and floating bridge inverters, respectively. The fundamental phase difference between  $\vec{v}_1$  and  $\vec{v}_2$  is denoted by the angle  $\alpha$ , see Fig. 2.4.

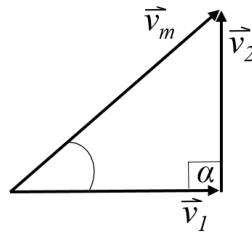


Fig. 2.4. The voltage phasors of the dual inverter drive

In the proposed control scheme presented in chapter 3,  $\alpha$  is kept constant at  $90^\circ$  such that the main converter and floating converter supply real and reactive power to the motor, respectively. However, other control methods may utilize  $\alpha$  as control parameter and employ a variable angle [24].  $\vec{v}_m$  is the per-phase fundamental RMS voltage supplied to the stator's windings, and is the vector sum of  $\vec{v}_1$  and  $\vec{v}_2$ :

$$|\vec{v}_1| = \frac{m_1 V_{dc}}{2\sqrt{2}} \quad (2.6)$$

$$|\vec{v}_2| = \frac{m_2 V_{cap}}{2\sqrt{2}} \quad (2.7)$$

$$\vec{v}_m = \vec{v}_1 + \vec{v}_2 \quad (2.8)$$

$V_{dc}$  and  $V_{cap}$  are the supply DC voltage and the floating capacitor's DC voltage, respectively. The amplitude modulation index of the main bridge is denoted by  $m_1$ , whereas the amplitude modulation index of the floating bridge is denoted by  $m_2$ . If not directly regulated, the voltage of the floating capacitor will naturally fluctuate and reach a steady-state level, related to the motor's load conditions: in steady-state, the stator's RMS current space-vector,  $\vec{i}_s$  in Figs. 2.5 and 2.6, is orthogonal to  $\vec{v}_2$ . Variations in the floating capacitor's voltage are dependent on the instantaneous real power absorbed by the floating bridge during system transients:

$$P_2 = 3|\vec{v}_2||\vec{i}_s| \cos \beta \quad (2.9)$$

Where  $\beta$  is the angle formed between vectors  $\vec{i}_s$  and  $\vec{v}_2$ . The DC link capacitance of the floating bridge may be made small enough as to meet the transient response requirements of the motor drive. A larger capacitance shows a smaller voltage variation and a more damped response for a given transient or disturbance. In other words, the floating capacitor size, along with a suitably tuned controller, can be selected so that the system's transient response is fast enough to cope with the motor's transients.

The current vector  $\vec{i}_s$  may be projected onto the axis of  $\vec{v}_2$  resulting in the real and imaginary components,  $i_{s,R}$  and  $i_{s,I}$ . Assuming an ideal capacitor and power electronics, if the system is operating at steady-state then the real component of  $\vec{i}_s$  will be zero:

$$i_{s,R}^{SS} = 0 \quad (2.10)$$

If a purely capacitive component is assumed then any real current being absorbed or produced by the floating bridge results in variance in the capacitor's voltage, hence a non-steady-state condition. However, under practical conditions the floating bridge will experience natural power losses such as cable conduction losses, the esr of the capacitor, as well as the switching and conduction losses of the power electronics. Thus, under steady-state these power losses result in the angle  $\beta$ , between  $\vec{i}_s$  and  $\vec{v}_2$ , to be slightly less than  $90^\circ$  (as a slight amount of real current is required). For the remainder of the discussion regarding the principles of operation and the proposed control scheme, these power losses will be neglected and  $\beta$  will be assumed to be  $90^\circ$  under steady-state operation.

The floating capacitor transient charging process is depicted by Fig. 2.5, assuming the angle  $\alpha$  is held constant at  $90^\circ$ , as is proposed by the controller presented in chapter 3.

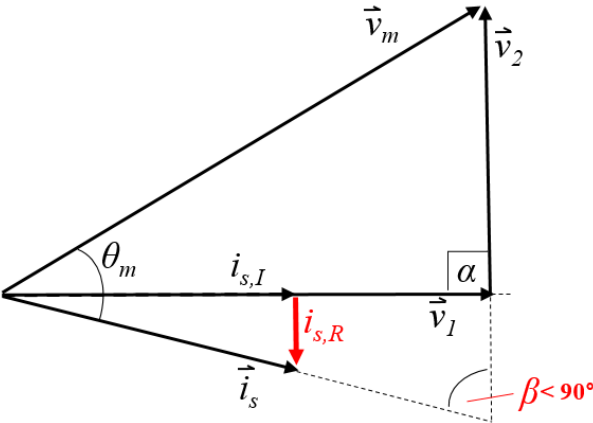


Fig. 2.5. The natural charging process of the floating capacitor

Where  $\theta_m$  is the power factor angle of the motor. Since  $\beta < 90^\circ$ ,  $P_2$  will be positive, thus real power is absorbed by the floating bridge and the capacitor charges. Therefore,  $|\vec{v}_2|$  will increase in a proportional manner to the capacitor's voltage. Assuming the power factor angle of the motor remains fixed,  $\vec{v}_m$  and  $\vec{i}_s$  will move counter-clockwise in the figure. This action will continue until  $i_{s,R}$  reaches a value of zero, corresponding to an angle  $\beta$  equal to  $90^\circ$ . The larger the difference between the angle  $\beta$  and  $90^\circ$ , the faster the rate of capacitor charging or discharging will be. The complementary discharging process of the floating capacitor is demonstrated by Fig. 2.6.

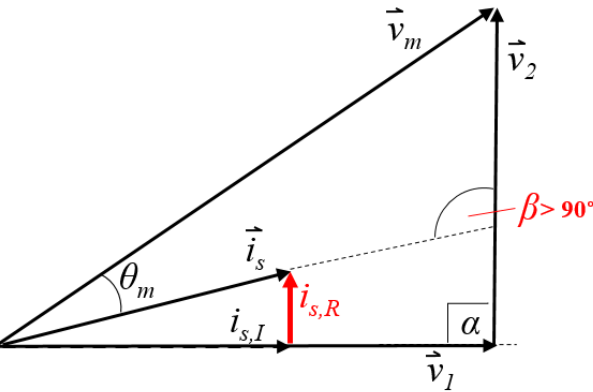


Fig. 2.6. The natural discharging process of the floating capacitor

Similarly, as  $\beta > 90^\circ$ ,  $P_2$  will be negative causing real power to be produced by the floating bridge while the capacitor discharges.  $|\vec{v}_2|$  will decrease in a proportional manner to the capacitor's voltage, moving  $\vec{v}_m$  and  $\vec{i}_s$  clockwise in the figure. Once again this action will continue until  $i_{s,R}$  equals zero and  $\beta$  equals  $90^\circ$ . It has been demonstrated, that if left unregulated the floating capacitor will naturally charge or discharge to a stable steady-state operating point depending on the motor's current loading conditions [22,23].

Three factors directly influence the angle  $\beta$ , and thus influence the steady-state voltage level of the floating capacitor: the fundamental phase angle difference between the two voltage injections ( $\alpha$ ), the power factor angle of the motor ( $\theta_m$ ), and the magnitude of the phasor  $\vec{v}_l$ . In the proposed control scheme presented in chapter 3,  $\alpha$  is kept constant at  $90^\circ$  as to improve the stability of the floating capacitor's voltage; however, different schemes may use a variable angle towards varying control objectives. The motor's power factor angle is not directly controllable, as it is highly dependent on the motor's external loading conditions, as well as the voltage supplied to the motor. Lastly, the magnitude of  $\vec{v}_l$  is proportional to the amplitude modulation index  $m_l$ . Therefore,  $m_l$  may be used as a control parameter to effectively regulate the floating bridge's capacitor voltage, and hence the output voltage  $|\vec{v}_2|$ . For example, if the system is operating as steady-state and the capacitor voltage is to be increased, then the value of  $m_l$  may be increased, hence increasing  $|\vec{v}_l|$ , see Fig. 2.5. This action causes the angle  $\beta$  to decrease slightly from  $90^\circ$ , as  $\vec{i}_s$  lags behind  $\vec{v}_l$ . With  $\beta$  less than  $90^\circ$ , real power will flow into the floating bridge and charge the capacitor according to (2.9). Conversely,  $m_l$ , and hence  $|\vec{v}_l|$ , may be decreased to lower the floating capacitor's voltage, see Fig. 2.6. These inherent operating principles arise from the topology of the DID system and were utilized in the development of the proposed control scheme, contributing to a non-complex constant motor power factor control algorithm without the use of feedback current measurements.

## Chapter 3

# Power Factor Control for High Motor Efficiencies

This chapter describes the proposed control scheme for the open-winding DID topology. Furthermore, justification for the constant motor power factor control method in a variable frequency drive is presented. The focus of the proposed controller is to maintain high motor power conversion efficiencies over a wide range of motor load settings and drive operating frequencies, while also providing voltage boosting for extending the constant torque region of the motor and improving performance in the speed range extension region. These benefits, along with the other inherent benefits of the selected topology, create an attractive motor drive system. Applications for the proposed control include variable-frequency variable-torque industrial drive applications such as fans, pumps, and compressors. As many industrial drives have high capacity factors and long lifetimes, it is imperative to maintain high efficiencies independent of operating point. In addition, the multilevel nature of this topology makes it suitable for medium and high power applications.

The floating bridge DID topology has been demonstrated to have high power conversion efficiencies when operating the motor with a constant power factor control [33]. The proposed controller builds upon the previous iteration with the following features: a non-complex control structure; minimal feedback signals; utilization of the DID's structure topology; and a variable floating bridge DC capacitor voltage that inherently changes with the motor's operating conditions, hence improving the overall drive's power conversion efficiency.

### **3.1 Achieving High Efficiencies at a Constant Power Factor**

Maximizing the power conversion efficiency of the induction motor has many benefits for improving the operational lifetime of the machine, and lowering the power drawn from the DC supply [34-37]. Oversizing motors in industry is a common practice which often leads to very low operating power factors and poor efficiencies [38]. In particular, an industry survey concluded that 29% of induction motors installed in 1992 were regularly operated at less than 50% load [39]. Therefore, a system which automatically operates the motor at its maximum efficiency point regardless of load could realize large energy saving and extend the lifetime of the machine.

The maximum motor operating efficiency can be linked to many potential control parameters, but for this work is linked to the machine operating with a constant power factor through controlling the motor's supply voltage [40,41]. Improving a motor's power factor through voltage variation is a well-known technique used to maintain reasonable motor slip throughout operation [40]. Furthermore, it has been demonstrated that using a constant displacement power factor control scheme over an entire operating range is an effective efficiency optimization strategy in medium sized industrial drives [41]. In simplistic terms, the magnetizing inductance of the induction motor is considered to be in parallel to the rotor circuit, which is largely resistive. Balancing the motor's magnetizing current with the torque producing rotor current, corresponds to a power factor of approximately 0.71. Motor voltage control (or scalar control) can improve the motor's power conversion efficiency by controlling its operating power factor; essentially controlling the balance between its iron and copper losses. While a constant power factor setpoint of 0.71 was selected for the test motor used in this work, the optimal power factor for minimizing overall losses throughout operation varies slightly between motors. High motor operating efficiencies can result from constant power factor control throughout a wide range of drive operating frequencies and load conditions.

Theoretical motor efficiencies at a constant power factor may be compared to the theoretical maximum possible efficiencies for the IM under various operating conditions based upon equivalent circuit model calculations. The applied equations are derived from the exact per-phase equivalent circuit model of the open-winding IM, see Fig. 3.1.

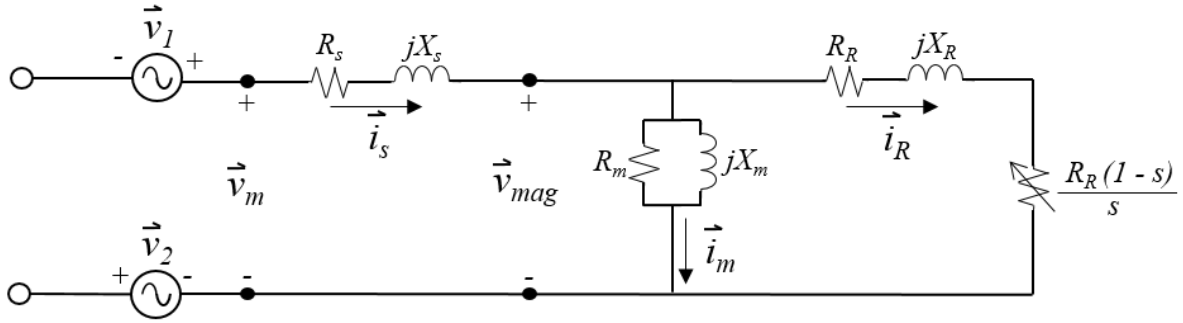


Fig. 3.1. The exact per-phase equivalent circuit model of the open winding induction motor

The stator impedance, magnetizing impedance, and rotor impedance of the above circuit are given by the following respective equations:

$$Z_s = R_s + jX_s \quad (3.1)$$

$$Z_m = \frac{j(R_m X_m)}{R_m + jX_m} \quad (3.2)$$

$$Z_R = \frac{R_R}{s} + jX_R \quad (3.3)$$

Therefore, the per-phase equivalent impedance of the induction motor as seen from the stator's terminals can be expressed by (3.4), and the machine's power factor may be found using (3.5).

$$Z_{ph} = \frac{Z_m Z_R}{Z_m + Z_R} + Z_s = R_{ph} + jX_{ph} \quad (3.4)$$

$$PF = \cos(\tan^{-1}(X_{ph} / R_{ph})) \quad (3.5)$$

The per-phase motor impedance can be used to calculate the total stator supply current as well as the portion of current supplied to the rotor, based on a given supply voltage.

$$\vec{i}_s = \frac{\vec{v}_m}{Z_{ph}} \quad (3.6)$$

$$\vec{i}_R = \frac{\vec{v}_m - \vec{i}_s Z_s}{Z_R} \quad (3.7)$$

The input power, output power, and machine efficiency of the open-winding IM may be found using (3.8), (3.9), and (3.10), respectively.

$$P_{in} = 3|\vec{i}_s|^2 R_{ph} \quad (3.8)$$

$$P_{out} = 3|\vec{i}_R|^2 \frac{R_R(1-s)}{s} \quad (3.9)$$

$$\eta = 100 \left( \frac{P_{out}}{P_{in}} \right) \quad (3.10)$$

Lastly, the three primary modes of loss in the ideal equivalent circuit model are stator copper loss, stator core loss or iron loss, and rotor copper loss, described by (3.11), (3.12), and (3.13), respectively, neglecting both the saturation effects within the motor and friction losses.

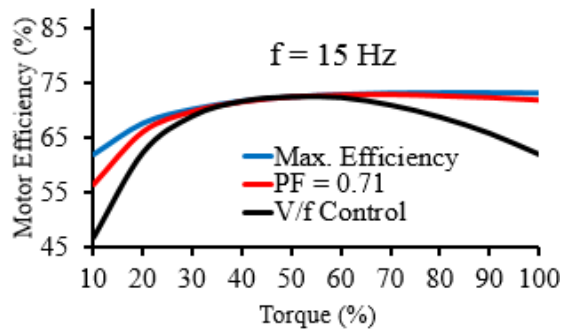
$$P_{s,loss} = 3|\vec{i}_s|^2 R_s \quad (3.11)$$

$$P_{core,loss} = 3 \left( \frac{|\vec{i}_m| |jX_m|}{|R_m + jX_m|} \right)^2 R_m \quad (3.12)$$

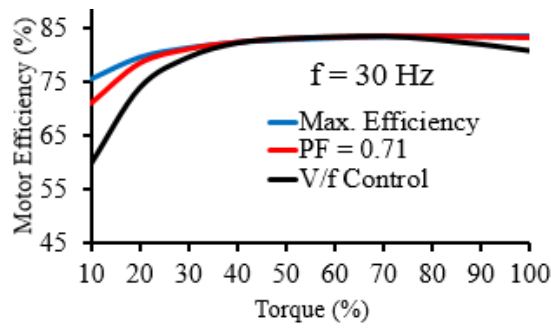
$$P_{R,loss} = 3|\vec{i}_R|^2 R_R \quad (3.13)$$

The listed equations may be utilized to conduct a spreadsheet analysis for any given motor, in order to characterize its performance at various operating points over a range of supply frequencies, loading conditions, and power factors.

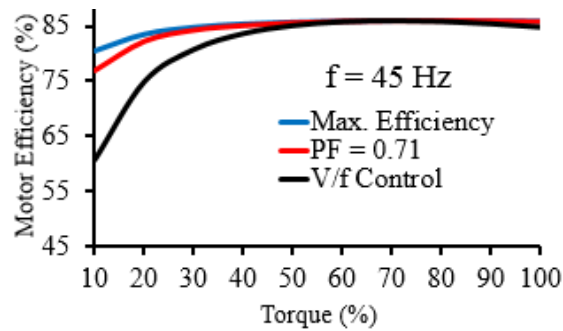
For a 5 HP experimental motor, Fig. 3.2 compares the theoretical efficiencies between using constant power factor control and the maximum possible motor operating efficiency. The theoretical efficiencies for various operating conditions and control methods were calculated using the exact equivalent circuit model described above, and the parameters for the motor used in this work. For the utilized motor, a constant power factor control of 0.71 achieves motor efficiencies very close to the maximum possible, with a deviation under light loads. For completeness, the two operating conditions in Fig. 3.2 are also compared with standard  $V/f$  control.



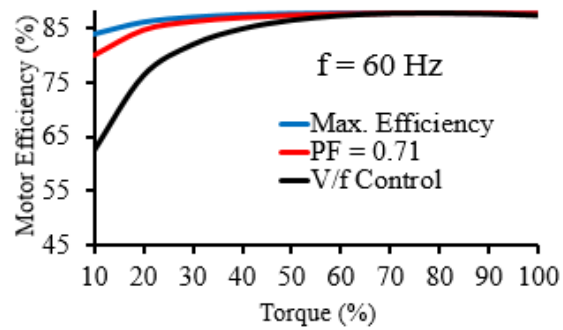
(a)



(b)



(c)



(d)

Fig. 3.2. Theoretical motor efficiencies (a) 15 Hz (b) 30 Hz (c) 45 Hz (d) 60 Hz

Fig. 3.3 displays the theoretical power factors that correspond to a maximum efficiency operation at the specified operating speed setpoints. A power factor of 0.71 is well within the range of optimal power factors. This value was selected, as opposed to the mean value from the optimal power factor range, as motor efficiency is more sensitive to power factor variation under light loads. These results justify the use of a relatively simplistic motor voltage control that keeps the motor operating at a constant power factor under variable frequency and variable load operation. The ideal constant power factor may vary slightly between induction motors, typically being near the range of 0.70-0.75. This control approach is very well suited for the drive structure being utilized: the DID topology with a floating capacitor bridge.

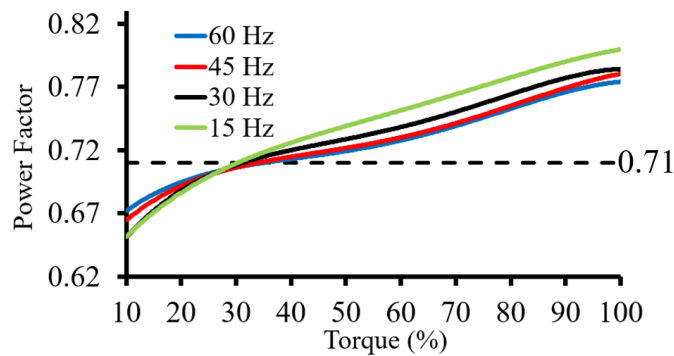


Fig. 3.3. Power factors for optimal efficiency operation for a 5 HP experimental motor

### 3.2 The Power Factor Controller for the Dual Inverter Drive

The proposed controller utilizes the inherent properties of the DID topology to implement a simple and effective method of constant power factor control. The controller keeps the angle  $\alpha$  at  $90^\circ$  for steady-state operation under all conditions. This results in the motor's stator current to be in phase with  $\vec{v}_1$  during steady-state, resulting in unity power factor operation of the main bridge, see Fig. 3.4.

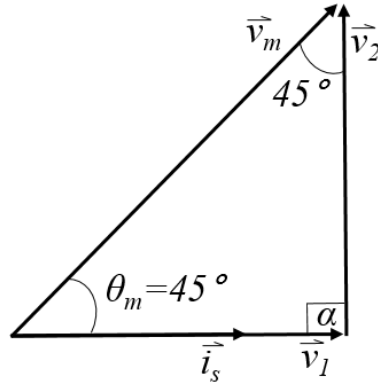


Fig. 3.4. Steady-state space-vector diagram for the proposed controller

The controller incorporates two cascaded PI compensators, see Fig. 3.5. The PI block in the “*slower*” outer control loop works to control the ratio between  $|\vec{v}_1|$  and  $|\vec{v}_2|$ : determined by measuring the DC voltages of both inverters and knowing their amplitude modulation indices  $m_1$  and  $m_2$ . The amplitude modulation index of the main bridge inverter,  $m_1$ , is controllable, while the floating bridge’s amplitude modulation index,  $m_2$ , is kept at its maximum value in order to minimize the floating capacitor’s voltage; thus, decreasing the switching losses and stresses in the secondary converter. A fixed ratio between  $|\vec{v}_1|$  and  $|\vec{v}_2|$  is maintained by regulating the reference signal  $V_{cap}^*$  for the floating capacitor’s voltage, which is limited between 0 and  $V_{dc}$ . This fixed ratio is determined by the reference motor power factor, which may be updated in the control scheme based upon the gain factor  $K$ :

$$K = 1/\tan[\cos^{-1}(PF^*)] \quad (3.14)$$

For the motor utilized in this work, the desired motor power factor angle is  $\theta_m=45^\circ$ , thus the value of the gain factor  $K$  equals 1, and the ratio of  $|\vec{v}_1|$  to  $|\vec{v}_2|$  is set to 1:1. However, this ratio could be altered in the control algorithm to obtain a wide range of desired motor power factors.

$V_{cap}^*$  provides the input signal to the “*faster*” inner control loop. The inner PI block minimizes the floating capacitor’s voltage error through controlling  $m_1$ : limited between 0 and 1.15. The magnitude of  $\vec{v}_1$  directly influences the charging and discharging of the floating capacitor. Equations in the Laplace domain for both PI compensators are as follows:

$$V_{cap}^* = (|\vec{v}_1| - K|\vec{v}_2|) \left( \frac{K_{p1}s + K_{i1}}{s} \right) \quad (3.15)$$

$$m_I = (V_{cap}^* - V_{cap}) \left( \frac{K_{p2}s + K_{i2}}{s} \right) \quad (3.16)$$

$K_{p1}$  and  $K_{p2}$  are the proportional gains and  $K_{i1}$  and  $K_{i2}$  are the integral gains for the primary and secondary PI compensators, respectively. Each compensator requires unique gains, as the bandwidth of the inner control loop must be large enough to track the output of the outer power factor control loop, while quickly rejecting disturbances in the capacitor's voltage. In other words, the inner loop gains are tuned according to the size of the floating capacitor and its corresponding  $dv/dt$  characteristics, whereas the outer loop gains are tuned according to the time constant of the motor and its dynamic response to load transients.

Under this control, and assuming ideal power electronics, the DID can boost the motor voltage 41% higher than when using a single bridge. However, the maximum practical motor voltage is limited by the internal flux saturation effects of the motor. This additional available voltage extends the base speed range of the drive and lessens the requirement for flux-weakening, thus allowing for higher torque production at high speeds, and better utilization of the motor's capabilities. In addition, the proposed control of  $V_{cap}$  effectively regulates the floating capacitor's voltage stability during transient load and frequency changes. Under light loads and low drive frequencies, the terminal motor voltage for the chosen nominal power factor is greatly reduced. Thus,  $V_{cap}^*$  is reduced automatically,  $m_I$  is reduced to track  $V_{cap}^*$ , and both  $|\vec{v}_1|$  and  $|\vec{v}_2|$  decrease in a proportional manner.



### 3.2.1 A Sensorless Method for Slip Compensation

As shown in Fig. 3.5, the motor's RPM reference is supplied to the control system, and is boosted by a slip frequency compensation value before being converted into a reference supply frequency. Constant motor power factor control enables a simple method for slip compensation, in which a motor-specific RPM compensation value may remain constant for all operation. Thus, the DID topology is well suited for slip frequency compensation, providing a method for more accurate speed control without using speed feedback measurements. For example, the test motor utilized in this work has a slip of 23 RPM while operating at a power factor of 0.71. Thus, by forcing the input power factor, and thus  $\theta_m$ , to be constant, the motor's slip frequency will also remain constant at all speed settings. Under experimental conditions, machine parameters will shift at varying temperatures caused by load fluctuations, thus creating small steady-state speed errors which vary over the load range. Lastly, an externally triggered integrator is utilized to produce the reference phase angles for both bridges, which are sent to the corresponding space-vector PWM modulators, see Fig. 3.5.

### 3.2.2 System Start-Up Procedure

The system start-up procedure is comprised of three individual stages. Firstly, the motor is started using a soft-start current-limiting method from solely the main converter, see Fig. 3.6. As the frequency is ramped up, the voltage supplied to the motor's terminals begins to ramp at a predetermined rate from zero volts to the desired voltage level upon start-up,  $v_{start}^*$ . During this process, the measured RMS motor current is compared to 150% of the motor's rated full-load current. If the measured current becomes greater than this threshold, the ramping of the supply voltage is paused until the measured current once again reaches acceptable levels. This method ensures the avoidance of large in-rush currents during motor start-up caused by acceleration torque. The three upper IGBT switches of the floating converter remain closed during this process, in order to emulate a Y-connection at the motor's secondary terminals. Secondly, switching in the floating converter is enabled and the capacitor is pre-charged to a pre-determined value using the second PI compensator of the control algorithm.

For example, under 60 Hz operation the magnitude of  $V_{cap}^*$  upon pre-charging was set to 100V. Lastly, the power factor control portion of the control scheme is enabled, thus allowing the first PI compensator to update  $V_{cap}^*$  appropriately corresponding to the drive's current frequency and load conditions.

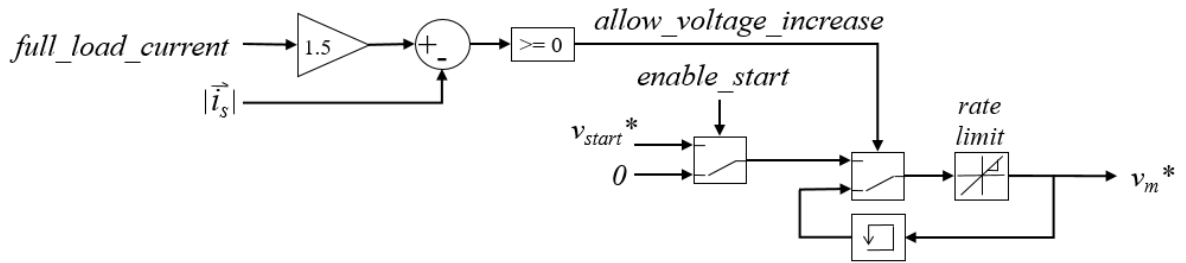


Fig. 3.6. Control block diagram of the soft-start algorithm

## Chapter 4

# System Results and Performance Analysis

The purpose of this chapter is to present the relevant simulation and experimental results for the proposed controller with the DID floating bridge topology, and to characterize its performance. Firstly, the hardware and software configuration used for the experimental testing will be described in detail. Numerical simulations were utilized to verify constant power factor operation and the regulation of the floating capacitor's voltage, using a variety of capacitances. The drive control proved to be effective by maintaining the nominal motor power factor of 0.71 for loads varying between zero and full load, and over a supply frequency range of 10-75 Hz. Experimentally, the conducted testing verifies and validates the benefits of running a 5 HP induction motor under constant power factor operation. Experimental results show both steady-state performance, and transient voltage and current waveforms. Steady-state efficiency measurements were obtained at four drive frequencies: 15, 30, 45, and 60 Hz. In addition to the steady-state benefits, the drive proved robust when subjected to a multitude of motor load and drive frequency transients. Other transient results presented include the reference and feedback voltage signals during the system start-up procedure.

## 4.1 Experimental Setup

Experimental testing was utilized to validate the proper operation of the proposed constant power factor controller, demonstrate the expected efficiency benefits of constant power factor operation, and show the robustness and stability of the drive throughout realistic load torque and supply frequency changes. The test motor used was a 4-pole, 230 V, 5 HP, 60 Hz, class H induction motor. Testing covered a range of frequencies between 10 and 70 Hz between no-load and full-load conditions. The rated nameplate parameters for the test motor are included in Table 4.1.

Table 4.1. Parameters of the test induction motor

$P_{rated}$	=	3.73 kW	$R_s$	=	0.300 $\Omega$
$T_{rated}$	=	20.34 Nm	$R_R$	=	0.244 $\Omega$
$I_{s,rated}$	=	13 A	$X_s$	=	0.697 $\Omega$
$V_{s,rated}$	=	230 V	$X_R$	=	0.544 $\Omega$
$f_s$	=	60 Hz	$X_M$	=	19.671 $\Omega$
$p$	=	2			

Custom power electronics used Semikron (SKiM306GD12E4) IGBT modules with a 4 mF floating capacitor. A 300 V Xantrex DC supply (XPR 300-20) was utilized to supply the main bridge. A MAGTROL dynamometer was used to load the motor with a specified torque setpoint, and the converters were controlled using the dSPACE DS1104 board with the controller implemented in Simulink, see Fig. 4.1. Continuous PWM at a switching frequency of 7.5 kHz was utilized with third-harmonic injection to achieve the classic double-humped space-vector PWM waveforms.

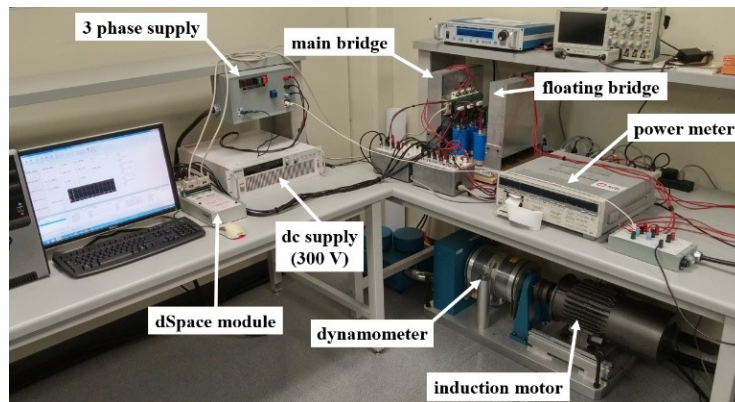


Fig. 4.1. Experimental setup

## 4.2 System Start-up

The conducted simulations were utilized to ensure the proper system start-up procedure, the limiting of the in-rush currents due to acceleration torque, and stability of the floating capacitor during pre-charging. Simulations assumed: an input DC supply voltage of 300 V, a floating capacitor of 1 mF, and a switching frequency of 7.5 kHz. Fig. 4.2 displays simulation results of the RMS motor voltage and current during the first stage of the system start-up procedure.

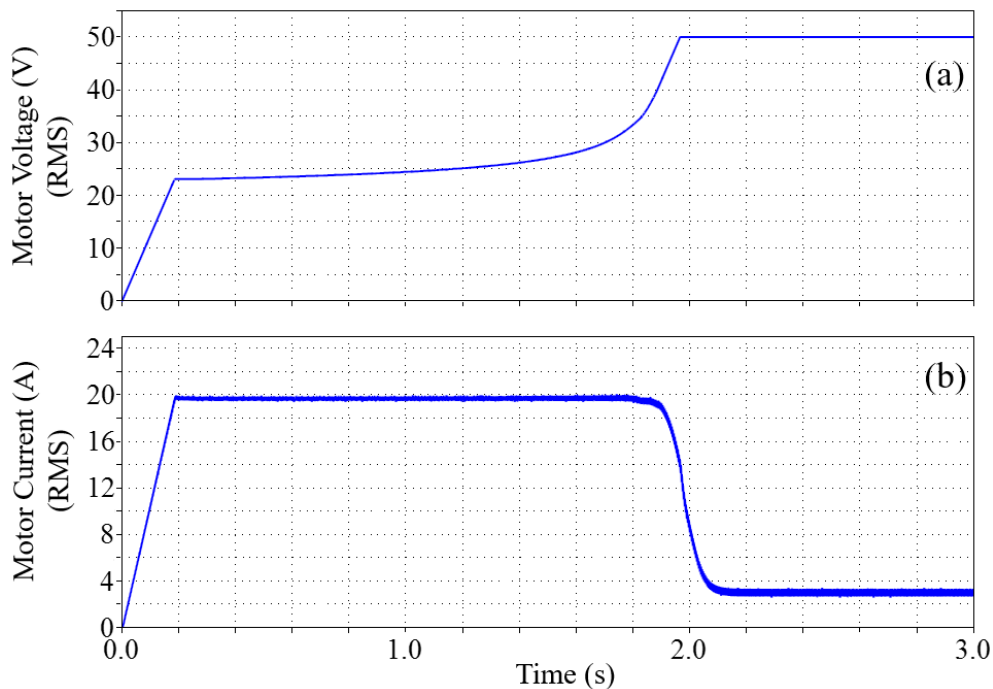


Fig. 4.2. Simulation results: (a) RMS motor voltage and (b) RMS motor current during soft-start

In Fig. 4.2, the starting voltage setpoint has been set to 50 V. Upon start-up, the controller begins to linearly increase the motor's supply voltage, until the measured and calculated RMS motor current reaches its threshold value, in this scenario 19.5 A. When the threshold value is reached, the increase in the supply voltage is paused until the measured current has once again reached an acceptable level. As the rotor overcomes its acceleration torque and gains speed, the current drawn by the motor is reduced and the voltage may continue ramping to its setpoint. This ensures no potentially damaging over-currents are experienced during start-up.

Once the motor has reached its desired speed, the second portion of the start-up procedure is enacted: pre-charging of the floating capacitor, see Fig.4.3.

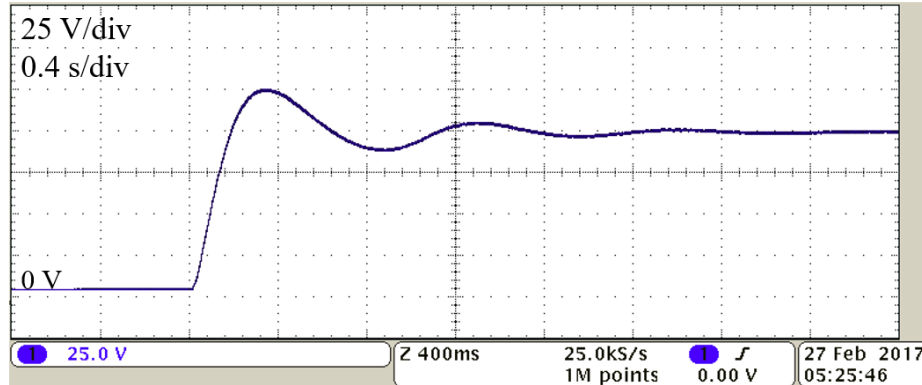
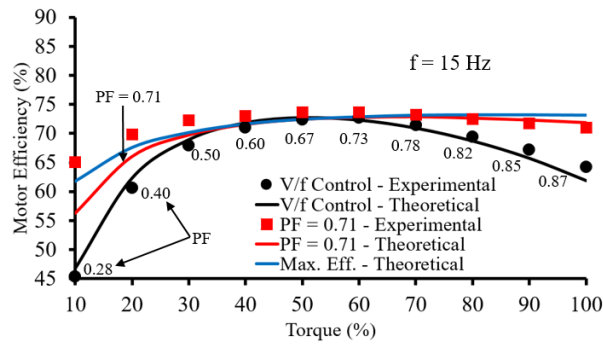


Fig. 4.3. Experimental results: capacitor pre-charging [4 mF floating capacitor]

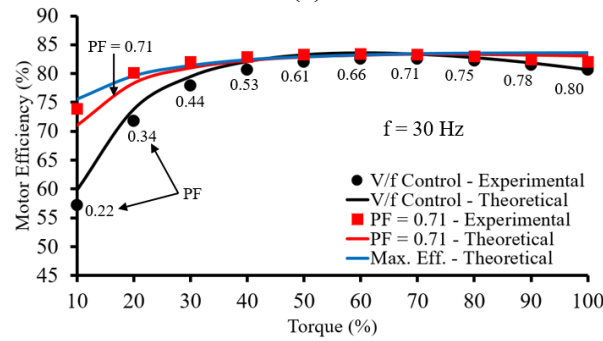
During the first stage of the drive’s start-up procedure, the three upper switches of the floating bridge remain closed, thus effectively creating a Y-connection. This causes the open-winding IM to behave in an identical fashion to a regular three-phase motor. Once the motor has reached speed, switching is enabled in the floating bridge with a modulation index,  $m_2$ , equal to 1.15, allowing current to charge the capacitor. The second PI compensator of the control algorithm is utilized to vary  $m_1$  such that the floating capacitor charges to a pre-determined setpoint, 100 V in Fig. 4.3. The fundamental phase angle difference,  $\alpha$ , remains at  $90^\circ$  during this process. Once the capacitor has reached a steady-state voltage level the first PI compensator of the control scheme is enabled, and the power factor of the motor is set to the desired value.

### 4.3 Steady-State System Performance

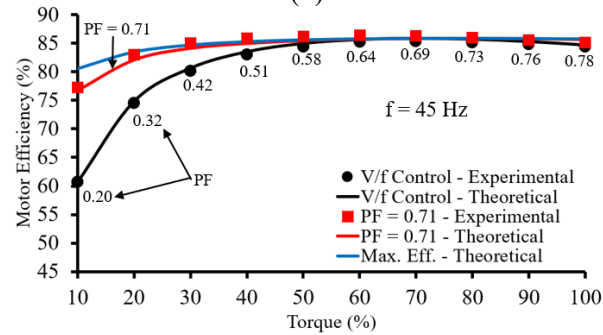
The motor’s power conversion efficiency was obtained at the four primary drive frequencies tested: 15, 30, 45, and 60 Hz. The motor efficiency is compared between the proposed constant power factor controller, maximum theoretical efficiency operation, and constant  $V/f$  control, see Fig. 4.4. For the purpose of this manuscript, conventional  $V/f$  control is utilized as a low benchmark standard, while the goal of the system is to achieve motor efficiencies close to the theoretical maximum values at various steady-state operating points.



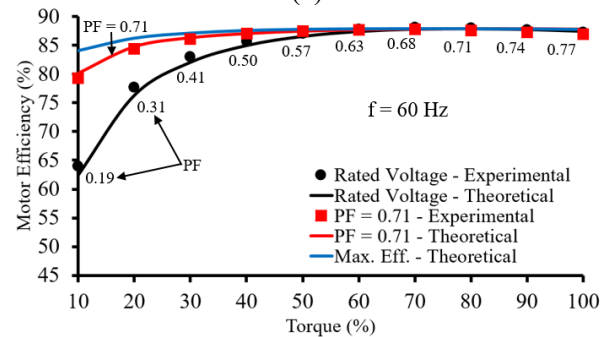
(a)



(b)



(c)



(d)

Fig. 4.4. Experimental results: motor efficiencies under  $V/f$  control and constant power factor control compared with the theoretical maximum efficiency (a) 15 Hz (b) 30 Hz (c) 45 Hz (d) 60 Hz

The theoretical maximum efficiencies were calculated using the exact equivalent circuit model for the induction motor, while accounting for thermal variations in the motor's resistive parameters across varying loading conditions. In order to account for these variations during experimental testing, the drive was run thirty minutes for each operating point and control method, to allow all measured parameters to settle to their steady-state values. The 300 V DC source utilized in the experimental setup was not sufficient to supply the motor its rated voltage under 60 Hz operation from a single inverter for standard  $V/f$  control, thus the motor was supplied directly at its rated voltage from a 60 Hz source with no power electronics in this scenario. However, the inherent voltage boosting capability of the DID enabled the use of the 300 V DC supply under constant power factor 60 Hz operation for all motor loads. This example further illustrates the usefulness of the DID's voltage boosting capability while operating from a limited DC supply voltage.

Firstly, the data shows good agreement between the theoretical and experimental results. Rated voltage  $V/f$  control results in large motor efficiency variations with load: drooping slightly at high loads, and with a significant decrease under light load conditions. The motor's power conversion efficiencies are highest under 60 Hz operation, and decrease with each drive frequency setting. The  $V/f$  efficiencies peak in the mid-torque regions, which coincide with the constant power factor controller operation curves. The constant power factor controller results in elevated motor efficiencies compared to  $V/f$  control, remaining fairly constant with load settings, before beginning to droop at approximately 30% load. The largest efficiency gains are observed under 15 Hz operation, for which constant power factor control shows increases over  $V/f$  control of approximately 18% and 7% at loading conditions of 10% and 100%, respectively. Most importantly, the motor efficiency remains very close to the theoretical maximum power conversion efficiencies. The largest discrepancies between the measured efficiency and the theoretical maximum efficiency occurred at 10% load during 45 Hz and 60 Hz operation, a roughly 4% decrease. Typically, properly sized industrial motors are not run at loads this far below the rated torque for extended periods. At the supply frequencies of 15 and 30 Hz there is an approximate 1.5% decrease in efficiency from the theoretical maximum at full load. These discrepancies are expected based upon theoretical predictions, as the optimal power factor is shown to vary over the operating range, see Fig. 3.3.

The measured experimental efficiencies improved relative to the theoretical values under low loads as the supply frequency was decreased. This is due to the approximation of the motor's parameters in the equivalent circuit model, and their fluctuation with thermal variation. As the frequency was reduced, the approximation relating temperature to resistivity became less accurate.

The current drawn by the motor also demonstrates the benefits of the proposed drive controller. At the four drive frequencies tested, the constant power factor control strategy results in a lower motor current than conventional  $V/f$  control at motor loads less than 60%, see Fig. 4.5.

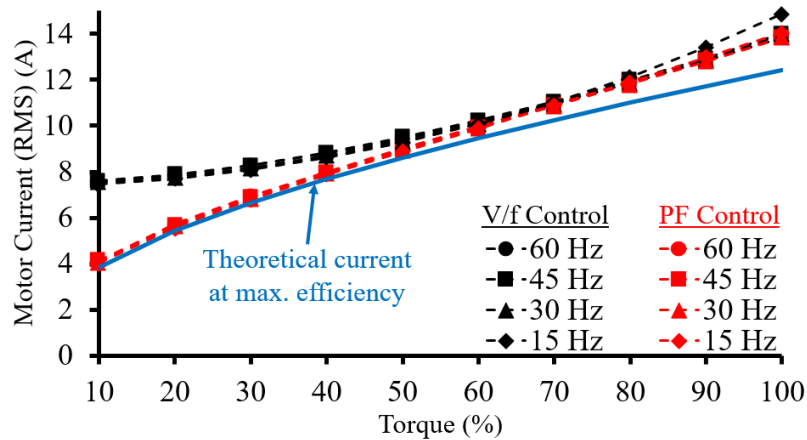


Fig. 4.5. Experimental results: motor current comparison between constant power factor control,  $V/f$  control, and the theoretical maximum efficiency operation

The greatest decrease in current magnitude is observed at 10% load, at which the motor current is reduced by nearly 4 A, resulting from the very poor power factors achieved at low loads resulting from  $V/f$  control. Furthermore, the constant power factor controller results in motor currents very close to the theoretical minimum values at below 60% load. At above 60% load, the equivalent circuit model utilized predicts motor currents slightly below the measured values, with a difference of 1.6 A at full load. Minimizing the motor current both decreases the conduction losses in the system and lowers the overall temperature of the motor.

Steady-state voltage measurements of the motor phase voltage and floating capacitor voltage demonstrate the action of the proposed controller, see Fig. 4.6. Under 60 Hz operation and at rated load, the controller supplied a voltage boost of 8% beyond the motor's rated

voltage in order to maintain the desired power factor (20% beyond the voltage capability of the single inverter drive). Thus, this topology can extend the base speed range of the drive and improve motor performance at high speeds compared to a single inverter drive. At reduced motor loads and drive operating frequencies,  $|\vec{v}_1|$  and  $|\vec{v}_2|$  are reduced in a proportional manner, through the reduction of  $m_I$  and  $V_{cap}$ . The proposed controller automatically reduces the motor supply voltage to maintain the desired operating power factor under light loads. Theoretical expected values for the motor phase voltage and floating capacitor voltage were calculated using the motor's equivalent circuit model and the drive's circuit topology, resulting in similar trends to the measured values.

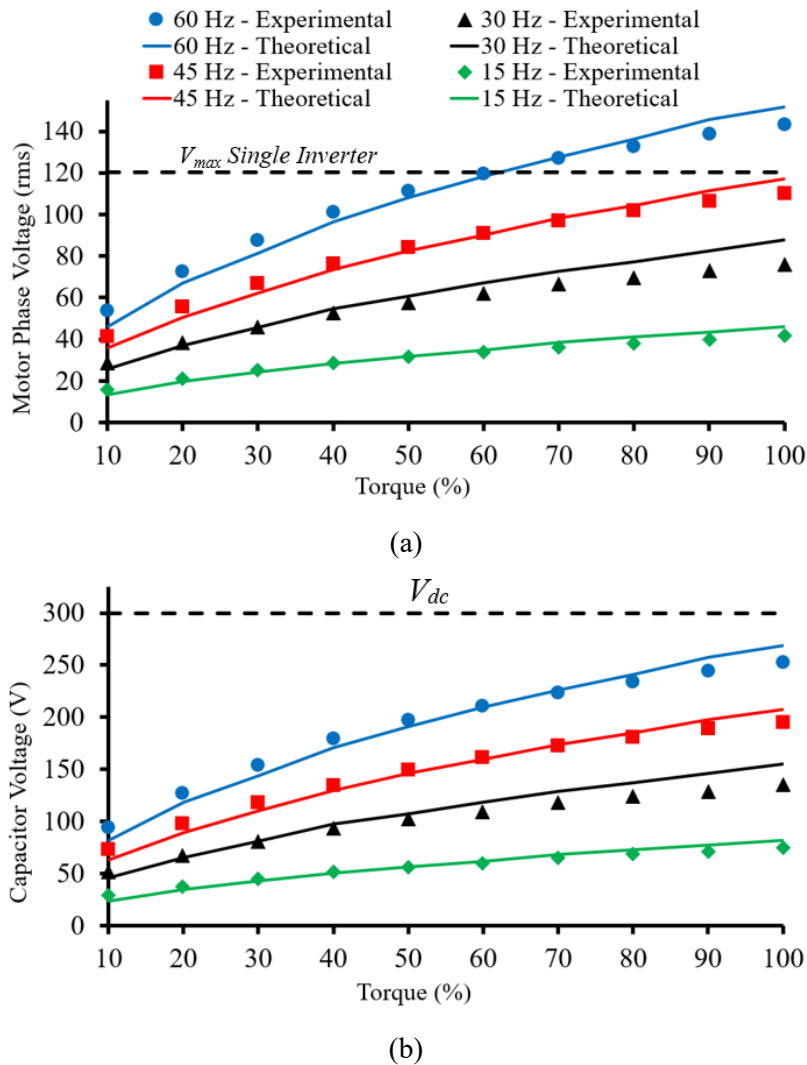


Fig. 4.6. Experimental results: (a) motor phase RMS voltage and (b) floating capacitor voltage of the dual inverter drive under constant power factor control

The motor's slip variation over the entire load range is greatly reduced under the proposed controller compared to the conventional  $V/f$  control scheme, see Fig. 4.7. Constant power factor operation results in a slip variation of approximately 10 RPM between ten percent and full load at each frequency setting.

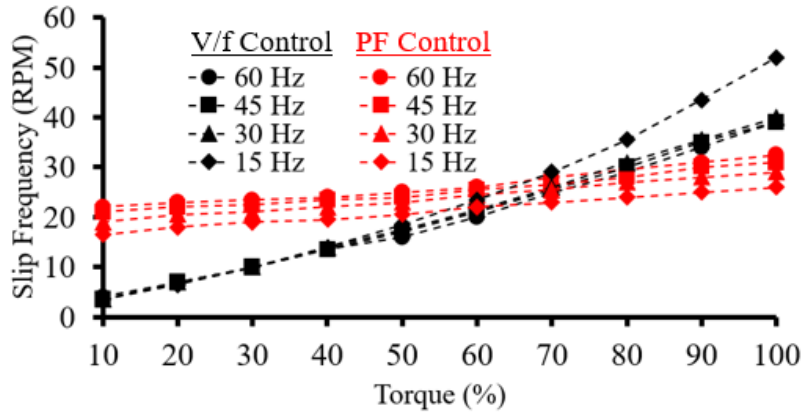


Fig. 4.7. Experimental results: motor RPM slip comparison between constant power factor control and  $V/f$  control methods

Theoretically, the motor slip remains constant across all motor loads while at a constant power factor; however, motor temperature fluctuations and varying switching losses in the power electronics result in small errors in the aforementioned steady-state assumptions. Essentially, the switching, conduction, and capacitor losses of the floating bridge cause the angle  $\beta$  between vectors  $\vec{i}_s$  and  $\vec{v}_2$  to be slightly less than  $90^\circ$ . Thus producing a non-zero  $i_{s,R}$  value at steady-state, and violating the assumption of (2.10). For the test motor utilized, a slip compensation value of 23 RPM (1.28% at rated speed) results in a maximum steady-state speed error of 7 RPM over all drive operating points tested, resulting in an error of 0.39% of the rated motor speed.

An additional benefit of lowering  $V_{cap}$  under light loads and low speeds is a reduction in the switching losses in the floating bridge. Device switching losses are proportional to both the device current and DC-link voltage. This reduction of  $V_{cap}$  lowers the switching losses in the electronics of the floating converter as compared to the main inverter, see Fig. 4.8.

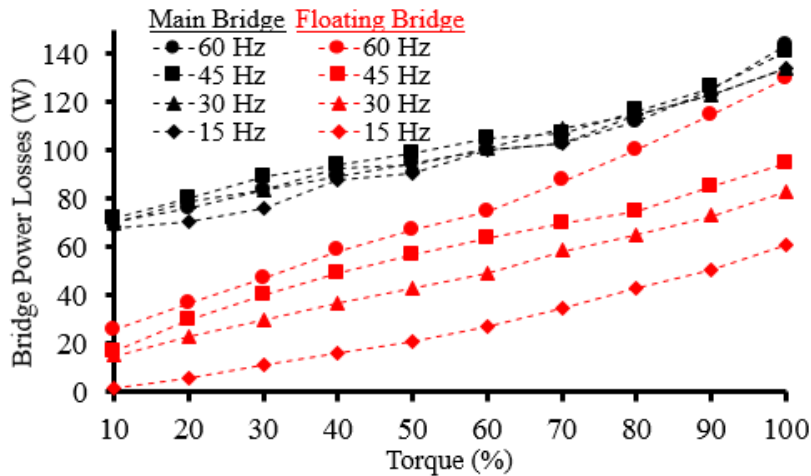


Fig. 4.8. Experimental results: power losses in the main and floating bridges

Due to mainly conduction losses, the power losses in the main bridge decrease with current almost linearly from full load to zero load for the four drive frequencies tested. However, in addition to varying with the load current, the losses in the floating bridge decrease significantly at each reduced frequency, primarily due to reduced switching losses from a reduced DC capacitor voltage. The difference in losses between the main and floating bridges represents a power savings due to the fluctuation of the floating capacitor's voltage, resulting in a more efficient system than if the floating capacitor remained equal to the DC-link voltage throughout all operation. This justifies maintaining the modulation index of the floating bridge at its maximum value for all operating points.

#### 4.4 System Performance During Load Transients

To demonstrate the controller's response to transient load changes, both simulation and experimental results are included for 0.5 per-unit positive and negative step changes in the motor's external load. Simulation results show the system's capacitor voltage, motor voltage, motor's power factor angle, and speed, see Fig. 4.9. Identical load step changes were applied to the experimental setup, demonstrating a stable floating capacitor voltage throughout the transient conditions, see Fig. 4.10.

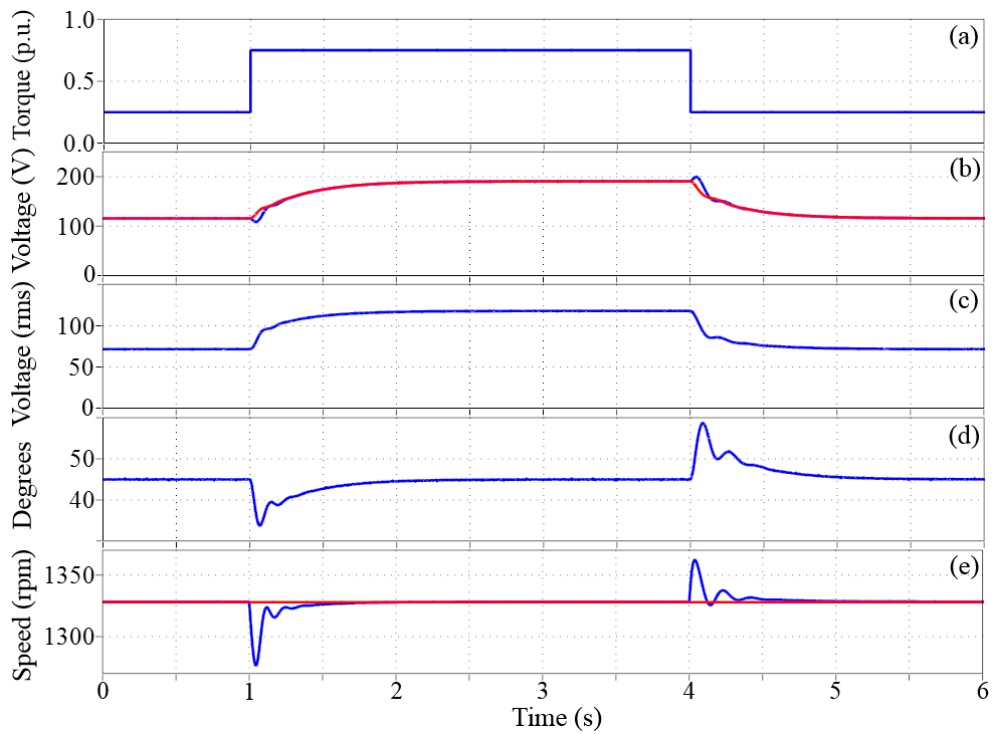


Fig. 4.9. Simulation results: (a) load torque; (b) capacitor voltage (blue) and reference (red); (c) motor phase voltage; (d) motor power factor angle; (e) motor speed (blue) and reference (red) [45 Hz; 1 mF floating capacitor]

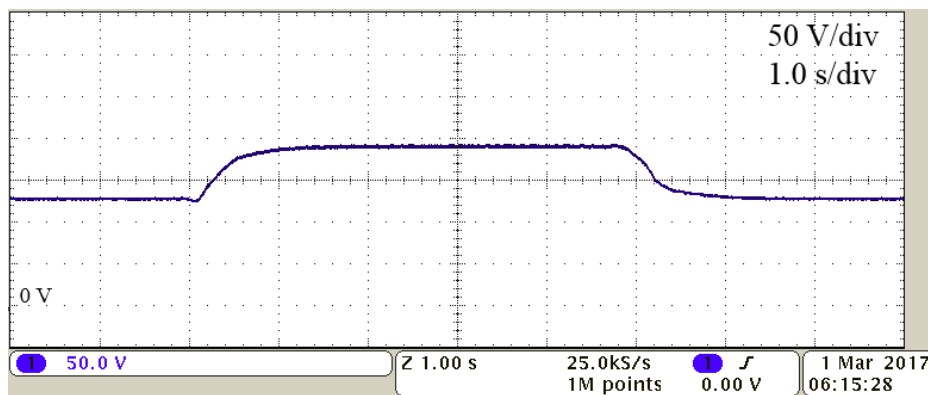


Fig. 4.10. Experimental results: floating capacitor voltage during load transients [45 Hz; 4 mF floating capacitor]

Further selected experimental results include the measured and calculated values of  $m_1$ ,  $|\vec{v}_1|$  and  $|\vec{v}_2|$ , and the RMS motor current,  $|\vec{i}_s|$ , see Fig. 4.11.

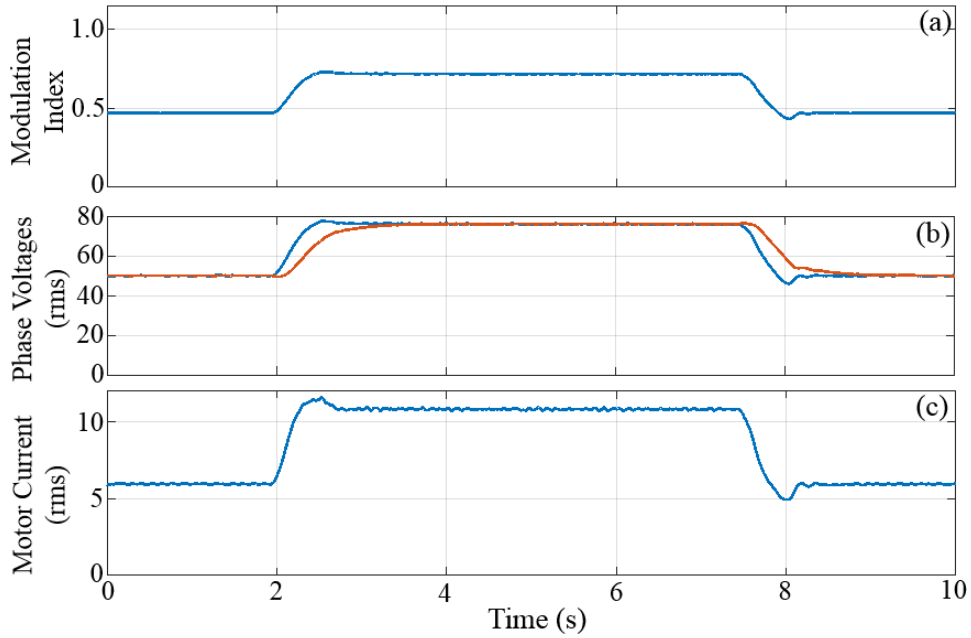


Fig. 4.11. Experimental results: (a) modulation index,  $m_1$ ; (b) phase voltages  $|\vec{v}_1|$  (blue) and  $|\vec{v}_2|$  (red); (c) RMS motor current,  $|\vec{i}_s|$  [45 Hz; 4 mF floating capacitor]

At the positive load step change,  $|\vec{v}_m|$  automatically increases to maintain the motor's nominal desired power factor. The first PI block increases  $V_{cap}^*$  to maintain the 1:1 ratio between  $|\vec{v}_1|$  and  $|\vec{v}_2|$ . The second PI block increases  $m_1$  to track  $V_{cap}^*$ , causing both  $|\vec{v}_1|$  and  $|\vec{v}_2|$  to increase. The motor's power factor angle and speed initially decrease after the load increase, before returning to the nominal values. Once the transient event has finished, the system will reach a new steady-state operating point, related to the new operating point, with a higher DC-link voltage at the floating bridge. The behaviour of the floating capacitor's voltage throughout the transient events demonstrates stable dynamic system performance.

## 4.5 System Performance During Speed Transients

Similarly, the system's response to speed transients is demonstrated through both simulation and experimental results. Fig. 4.12 shows simulation results for the motor's input reference speed, capacitor voltage, motor phase voltage, and power factor angle.

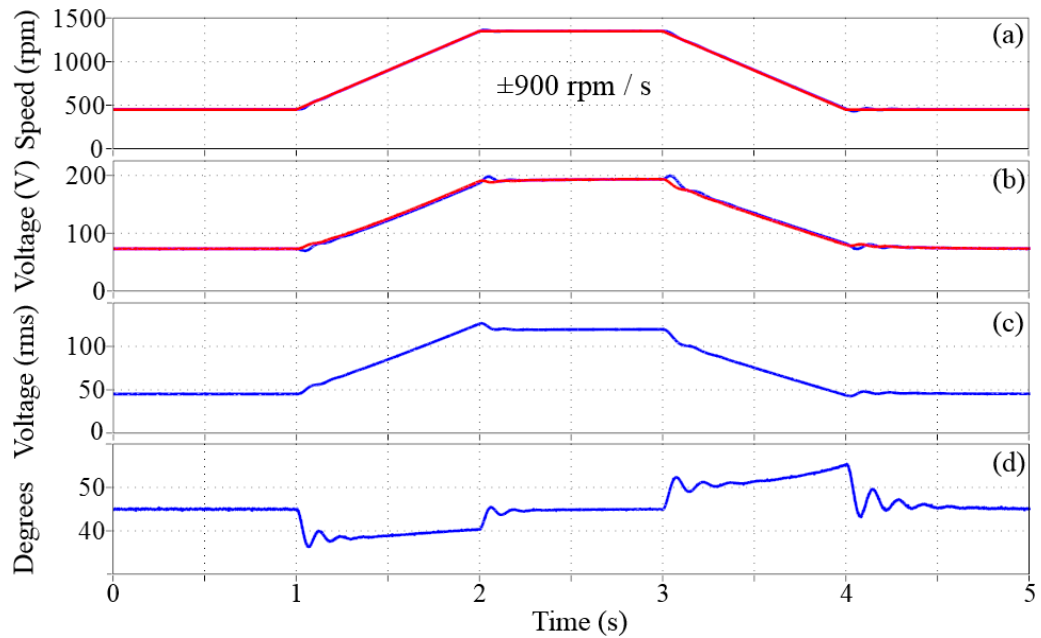


Fig. 4.12. Simulation results: (a) motor speed (blue) and reference (red); (b) capacitor voltage (blue) and reference (red); (c) motor phase voltage; (d) motor power factor angle [0.75 p.u. load; 1 mF floating capacitor]

Identical speed transients were applied to the experimental system, demonstrating a stable capacitor voltage throughout the speed transients, see Fig. 4.13.

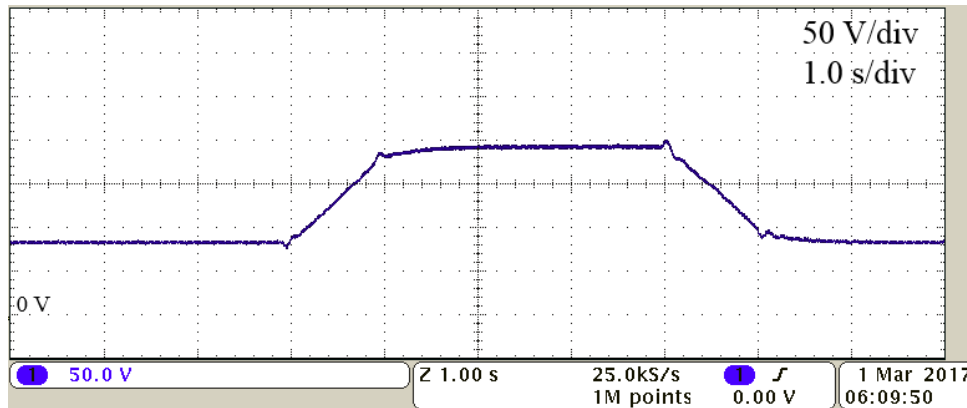


Fig. 4.13. Experimental results: floating capacitor voltage during speed transients [0.75 p.u. load; 4 mF floating capacitor]

Further selected experimental results include the calculated and measured values of  $m_l$ ,  $|\vec{v}_1|$  and  $|\vec{v}_2|$ , and the RMS motor current,  $|\vec{i}_s|$ , see Fig. 4.14.

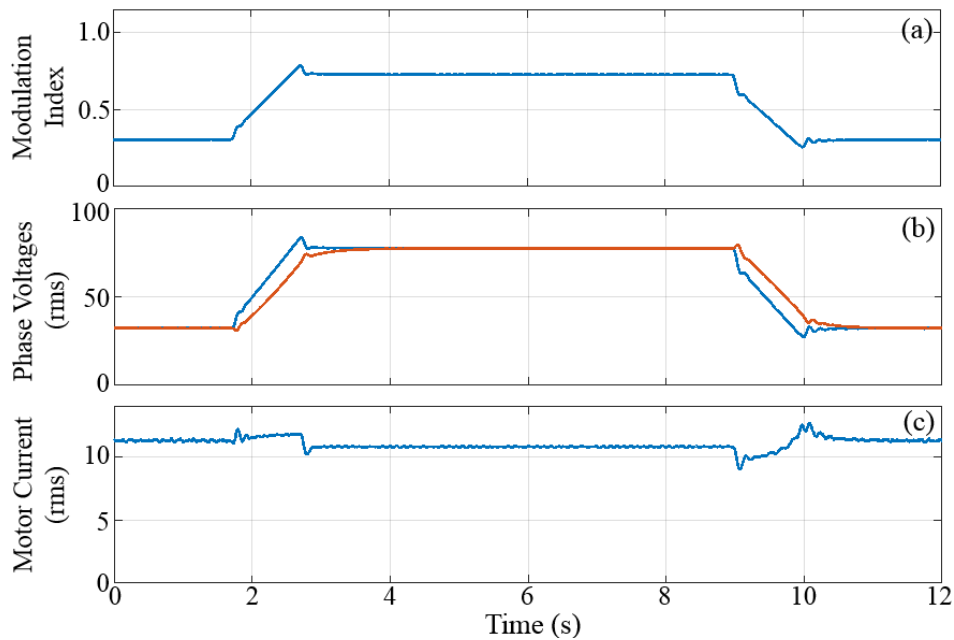


Fig. 4.14. Experimental results: (a) modulation index,  $m_l$ ; (b) phase voltages  $|\vec{v}_1|$  (blue) and  $|\vec{v}_2|$  (red); (c) RMS motor current,  $|\vec{i}_s|$  [0.75 p.u. load; 4 mF floating capacitor]

As the reference speed increases, the first PI block increases  $V_{cap}^*$  linearly to maintain the desired optimal motor power factor. The second PI block tracks  $V_{cap}^*$  through varying the amplitude modulation index of the main bridge,  $m_l$ . The motor's power factor angle is not maintained at the desired  $45^\circ$  during the speed transients, due to the inherent dynamic characteristic response of the motor, and the limitations of PI compensators in tracking ramping functions. Once the speed transient is complete, the floating capacitor settles at a new steady-state voltage, and the motor's nominal power factor is once again achieved. The system is shown to remain stable and responsive throughout the speed transients.

## Chapter 5

### Conclusion

The proposed drive control is successfully demonstrated for an open-winding induction motor drive system, using a dual inverter drive with a floating capacitor bridge. The system incorporates the inherent benefits of the dual inverter drive topology, including multilevel PWM and an extension of the motor's constant torque region through voltage boosting. These benefits are paired with the high-efficiency control method of constant power factor control. The novel controller maintains the motor's nominal power factor constant over a wide range of loading conditions and drive frequencies, with the purpose of maintaining high motor power conversion efficiencies for all operation. Furthermore, the controller regulates the floating capacitor's voltage to minimize high-frequency voltage fluctuations and maintain system stability. The addition of the floating capacitor bridge eliminates the pathways for zero-sequence circulating currents within the system. The system was examined using numerical simulations, theoretical calculations based on the induction motor's equivalent circuit model, and experimentally with a 5 HP test motor. Theoretical calculations justified the investigation of a constant power factor control scheme due to near-optimal expected efficiencies, and simulation tools were utilized to design and tune the presented control method. Experimental testing of the controller verified near optimal motor efficiencies over a wide load range, and showed large efficiency gains when compared to a constant  $V/f$  control scheme. The experimental results showed good agreement with the expected theoretical values. Furthermore, the proposed control was shown to be robust and stable throughout both motor

load and speed transients while utilizing a 4 mF floating capacitor, in terms of both motor operation and capacitor voltage stability. Thus, demonstrating good suitability for dynamic industrial drives. Steady-state performance for the proposed controller, regarding motor efficiency and maximum torque-per-amp, is very close to the optimal performance achievable with a more complex field-oriented current control approach with detailed machine characterization. Therefore, the presented non-complex and robust system is an attractive option for medium and high power multilevel drive applications, such as pumps, mixers, and compressors.

The proposed controller maintains a constant  $90^\circ$  phase angle difference between the voltages of the primary and secondary bridges for all operation, while the ratio between the magnitudes of these voltages controls the motor's power factor. The amplitude modulation index of the floating bridge is kept at its maximum value for all operation to avoid unnecessary over-charging of the floating capacitor. Varying the voltage reference signal of the floating capacitor significantly reduced the switching losses of the floating bridge at low speeds and light loads, thus further improving the system's overall power conversion efficiency. For example, at 30 Hz and 50% load, the overall power losses in the floating bridge were reduced by over 50%. In addition, the dual inverter drive topology was shown to be well-suited for slip frequency compensation, providing a method for more accurate speed control without using any speed feedback measurements. In particular, the constant slip frequency compensation method, incorporating a motor-specific RPM value, allowed for sensorless speed regulation of the open-winding induction motor within 0.39% of the rated motor speed for all drive operating points tested. The benefits of the proposed constant power factor controller, coupled with the inherent benefit of the DID floating bridge topology, make this system a viable system for industrial multi-level motor drive applications.

## **5.1 Suggestions of Future Work**

Future work regarding the proposed system could come in three primary areas. Firstly, a study could be conducted into the operation of the proposed controller in the field-weakening region. The experimental results included in this thesis demonstrate the voltage boosting

capability of the dual inverter drive under high torques at the rated motor frequency, up to 8% beyond the rated motor voltage and 20% beyond the capability of a single inverter drive. The implemented controller was able to provide the desired motor power factor under full load and rated speed. However, theoretical and experimental results were not included for the speed range extension region, beyond rated speed, as the scope of this work was efficiency optimization in the base speed range. In summary, the desired motor power factor can be maintained above base speed until the main inverter voltage reaches saturation. Above this threshold speed a variety of options are possible regarding how the controller responds to the system. One option is to allow the motor power factor to be decreased to maintain the motor at full flux; hence, lessening flux-weakening requirements and allowing for improved performance at high speeds. Alternatively, the maximum allowable torque limit for the motor may be reduced in order to maintain the constant power factor into the field-weakening region. A variable fundamental phase angle difference,  $\alpha$ , could also potentially be utilized for increased voltage boosting and improved performance at high speeds.

Secondly, the dynamic characteristics of the drive could be improved using a variety of current-control methods in a  $dq$  rotating frame of reference. The proposed control algorithm is well-suited to be extended to a more complex rotor field-oriented control scheme. In such a system, the motor's displacement power factor and flux could be controlled directly by the injected stator currents, as opposed to being controlled indirectly by the ratio of the fundamental bridge voltages. A small-signal model analysis of the floating bridge topology with a field-oriented control scheme could be utilized to accurately tune the system's gains for optimal dynamic performance. Thus, the knowledge of the rotor's position could potentially facilitate the further enhancement of the drive's dynamic characteristics while maintaining high motor efficiencies.

Lastly, as PWM techniques were not the focus of this work, a more in-depth analysis could be conducted into the various methods to achieve five-level PWM with the dual inverter drive topology, in conjunction with the constant power factor controller. The fundamental phase angle difference between the two inverters introduces an additional level of complexity to the continuous PWM method, as the voltage pulses from both bridges must be aligned to

achieve five-level waveforms. This can be achieved through applying the correct phase shift to the PWM carrier waveform of the floating bridge. Additionally, discrete space vector PWM could be applied with the constant power factor controller, using the PWM switching states to regulate the charging and discharging of the floating capacitor during each switching cycle. This method could potentially de-couple the voltage of the floating capacitor from the amplitude modulation index of the main bridge. It is clear that the DID topology with a floating bridge is an incredibly flexible motor drive system, allowing for a multitude of control techniques and operating objectives.

## References

- [1] U.S. Department of Energy, *Improving Motor and Drive System Performance: A Sourcebook for Industry*. Washington, DC: Office of Energy Efficiency and Renewable Energy, 2014.
- [2] B.K. Bose, “The past, present, and future of power electronics,” in *IEEE Ind. Elec. Magazine*, vol. 3, no. 2, pp. 7-11,14, June 2009.
- [3] ABB, “Energy efficiency makes a difference,” *ABB*. [Online]. Available: [http://www02.abb.com/db/db0003/db002698.nsf/0/a3881ed5c3dbc647c12575080036dafd/\\$file/energy\\_efficiency\\_makes\\_difference\\_191108.pdf](http://www02.abb.com/db/db0003/db002698.nsf/0/a3881ed5c3dbc647c12575080036dafd/$file/energy_efficiency_makes_difference_191108.pdf). [Accessed Sept. 12, 2017].
- [4] ABB, “Technical guide No. 4 – Guide to variable speed drives,” *ABB*, 2011. [Online]. Available: [https://library.e.abb.com/public/d3c711ec2acddb18c125788f002cf5da/ABB\\_Technical\\_guide\\_No\\_4\\_REVC.pdf](https://library.e.abb.com/public/d3c711ec2acddb18c125788f002cf5da/ABB_Technical_guide_No_4_REVC.pdf). [Accessed Sept. 12, 2017].
- [5] H. Lendenmann, R. Moghaddam, A. Tammi, and L.E. Thand, “Motoring Ahead,” *ABB Review 1/2011*, pp. 56-61, 2011.
- [6] B.K. Bose, “Power electronics and motor drives – recent progress and perspective,” *IEEE Trans. Ind. Electron.*, vol. 56, no. 2, pp. 581-588, Aug. 2008.
- [7] S. Chowdhury, P. Wheeler, C. Patel, and C. Gerada, “A multilevel converter with a floating bridge for open-ended winding motor drive applications,” *IEEE Trans. Ind. Electron.*, vol. 63, no. 9, pp. 5366-5375, May 2016.
- [8] S. Chowdhury, P. Wheeler, C. Gerada, and C. Patel, “Model predictive control for a dual-active bridge inverter with a floating bridge,” *IEEE Trans. Ind. Electron.*, vol. 63, no. 9, pp. 5558-5568, May 2016.
- [9] S. Chowdhury, P. Wheeler, C. Gerada, and S. Arevalo, “A dual inverter for an open end winding induction motor drive without an isolation transformer,” in *IEEE Applied Power Electron. Conf. and Expo. APEC*, 2015, pp. 283-289.
- [10] S. Chowdhury, P. Wheeler, C. Gerada, and C. Patel, “A dual two-level inverter with a single source for open end winding induction motor drive application,” in *Euro. Conf. on Power Electron. And App. EPE-ECCE-Europe*, 2015, pp. 1-9.

- [11] H. Kubo, Y. Yamamoto, T. Kondo, K. Rajashekara, and B. Zhu, "Zero-sequence current suppression for open-end winding induction motor drive with resonant controller," in *IEEE Applied Power Electron. Conf. and Expo. APEC*, 2016, pp. 2788-2793.
- [12] V. Oleschuk, V. Ermuratski, F. Profumo, A. Tenconi, R. Bojoi, and A.M. Stankovic, "Novel schemes of synchronous PWM for dual inverter-fed drives with cancellation of the zero sequence currents," in *IEEE Int. Symp. Power Electron., Electrical Drives Automation and Motion SPEEDAM*, 2006, pp. 451-456.
- [13] K. Ramachandrasekhar, S. Mohan, and S. Srinivas, "An improved PWM for a dual two-level inverter fed open-end winding induction motor drive," in *Int. Conf. on Electrical Machines ICEM*, 2010, pp. 1-6.
- [14] V.T. Somasekhar, S. Srinivas, B.P. Reddy, C.N. Reddy, and K. Sivakumar, "Pulse width-modulated switching strategy for the dynamic balancing of zero-sequence current for a dual-inverter fed open-end winding induction motor drive," *IET Electric Power Applications*, vol. 1, no. 4, pp. 591-600, Jul. 2007.
- [15] Y. Zhao and T. Lipo, "Space vector PWM control of dual three-phase induction machine using vector space decomposition," *IEEE Trans. Industry App.*, vol. 31, no. 5, pp. 1100-1109, Sep. 1995.
- [16] D. Casadei, G. Grandi, A. Lega, C. Rossi, and L. Zarri, "Switching technique for dual-two level inverter supplied by two separate sources," in *IEEE Applied Power Electron. Conf. and Expo. APEC*, 2007, pp. 1522-1528.
- [17] G. Grandi and D. Ostojic, "Dual inverter space vector modulation with power balancing capability," in *IEEE EUROCON*, 2009, pp. 721-728.
- [18] D. Casadei, G. Grandi, A. Lega, and C. Rossi, "Multilevel operating and input power balancing for a dual two-level inverter with insulated DC sources," *IEEE Trans. Ind. App.*, vol. 44, no. 6, pp. 1815-1824, Nov. 2008.
- [19] E.G. Shivakumar, K. Gopakumar, S.K. Sinha, A. Pittet, and V.T. Ranganathan, "Space vector PWM control of dual inverter fed open-end winding induction motor drive," in *IEEE Applied Power Electron. Conf. and Expo. APEC*, 2001, pp. 399-405.
- [20] J. Kalaiselvi, K.R. Sekhar, and S. Srinivas, "Common mode voltage elimination PWMs for a dual two-level VSI with single inverter switching," in *IEEE Int. Symp. Ind. Electron. ISIE*, 2012, pp. 234-239.
- [21] A. Edpuganti and A. Rathore, "New optimal pulsewidth modulation for single dc-link dual-inverter fed open-end stator winding induction motor drive," *IEEE Trans. Power Electron.*, vol. 30, no. 8, pp. 4386-4393, Aug. 2015.
- [22] J. Ewanchuk, J. Salmon, and C. Chapelsky, "A method for supply voltage boosting in an open-ended induction machine using a dual inverter system with a floating capacitor bridge," *IEEE Trans. Power Electron.*, vol. 28, no. 3, pp. 1348-1357, Mar. 2013.

- [23] J. Ewanchuk and J. Salmon, "A square-wave controller for high speed induction motor drive using a three phase floating bridge inverter," in *IEEE Energy Conv. Cong. and Expo. ECCE*, 2010, pp. 2584-2591.
- [24] R. Haque, A. Kowal, J. Ewanchuk, A. Knight, and J. Salmon, "PWM control of a dual inverter drive using an open-ended winding induction motor," in *IEEE Applied Power Electron. Conf. and Expo. APEC*, 2013, pp. 150-156.
- [25] B.A. Welchko, T.A. Lipo, T.M. Jahns, and S.E. Schulz, "Fault tolerant three-phase AC motor drive topologies: a comparison of features, cost, and limitations," *IEEE Trans. Power Electron.*, vol. 19, pp. 1108-1116, Jul. 2004.
- [26] E. Levi, "Multiphase electric machines for variable-speed applications," *IEEE Trans. Ind. Electron.*, vol. 55, no. 5, pp. 1893-1909, Apr. 2008.
- [27] S. Kouro, J. Rodriguez, W. Bin, S. Bernet, and M. Perez, "Powering the future of industry: high-power adjustable speed drive topologies," *IEEE Industry App. Mag.*, vol. 18, no. 4, pp. 26-39, May 2012.
- [28] E. Levi, M. Jones, and W. Satiawan, "A multiphase dual-inverter supplied drive structure for electric and hybrid electric vehicles," in *IEEE Vehicle Power and Prop. Conf. VPPC*, 2010, pp. 1-7.
- [29] N. Bodo, M. Jones, and E. Levi, "PWM techniques for an open-end winding fivephase drive with a single DC source supply," in *IEEE Conf. on Ind. Electron. Soc. IECON*, 2012, pp. 3641-3646.
- [30] M.R. Baiju, K.K. Mohapatra, R.S. Kanchan, and K. Gopakumar, "A dual two-level inverter scheme with common mode voltage elimination for an induction motor drive," *IEEE Trans. Power Electron.*, vol. 19, no. 3, pp. 794-805, May 2004.
- [31] M. Mengoni, A. Tani, L. Zarri, G. Rizzoli, G. Serra, and D. Casadei, "Control of an open-ended induction machine using a dual inverter system with a floating capacitor bridge," in *IEEE Energy Conv. Cong. And Expo. ECCE*, 2015, pp. 4872-4879.
- [32] M. Mengoni, A. Amerise, L. Zarri, A. Tani, G. Serra, and D. Casadei, "Robust control of an open-ended induction motor drive with a floating capacitor bridge over a wide speed range," in *IEEE Energy Conv. Cong. And Expo. ECCE*, 2016, pp. 1-7.
- [33] I. Smith, R.U. Haque, A. Tavakoli, and J. Salmon, "Power factor control for high efficiency operation of an open-ended winding motor using a dual inverter drive with a floating bridge," in *IEEE Applied Power Electron. Conf. and Expo. APEC*, 2017, pp. 1935-1941.
- [34] J. Kim, J. Jung, and K. Nam, "Dual-inverter control strategy for high-speed operation of EV induction motors," *IEEE Trans. Ind. Electron.*, vol. 51, no. 2, pp. 312-320, Apr. 2004.
- [35] J.S. Park and K. Nam, "Dual inverter strategy for high speed operation of HEV permanent magnet synchronous motor," in *IEEE Industry App. Conf. IAS*, 2006, pp. 488-494.

- [36] I. Tamrakar and O.P. Malik, "Power factor correction of induction motors using PWM inverter fed auxiliary stator winding," *IEEE Trans. Energy Conv.*, vol. 14, no. 3, pp. 426-432, Sep. 1999.
- [37] Y. Yao, A. Cosic, and C. Sadarangani, "Power factor improvement and dynamic performance of an induction machine with a novel concept of a converter-fed rotor," *IEEE Trans. Energy Conv.*, vol. 31, no. 2, pp. 769-775, Jun. 2016.
- [38] P. Pillay, "Applying energy-efficient motors in the petrochemical industry," *IEEE Industry App. Magazine*, vol. 3, no. 1, pp. 32-40, Jan. 1997.
- [39] E.B. Agamloh, "The partial-load efficiency of induction motors," *IEEE Trans. Industry App.*, vol. 45, no. 1, pp. 332-340, Jan. 2009.
- [40] R. Spee and A.K. Wallace, "Comparative evaluation of power factor improvement techniques for squirrel cage induction motors," *IEEE Trans. Industry App.*, vol. 28, no. 2, pp. 381-386, Mar. 1992.
- [41] F. Abrahamsen, F. Blaabjerg, J.K. Pedersen, and P.B. Thoegersen, "Efficiency-optimized control of medium-size induction motor drives," *IEEE Trans. Industry App.*, vol. 37, no. 6, pp. 1761-1767, Nov. 2001.